2018-01-01

# Assessing Corrosivity of Galvanized Soil Reinforcements from Electrochemical Tests

Diana Alejandra Cabrera
*University of Texas at El Paso*, dacabrera@miners.utep.edu

# ASSESSING CORROSIVITY OF GALVANIZED SOIL REINFORCEMENTS FROM ELECTROCHEMICAL TESTS

DIANA ALEJANDRA CABRERA

Master's Program in Civil Engineering

APPROVED:

Soheil Nazarian, Ph.D., CO-Chair

W. Shane Walker, Ph.D., CO-Chair

Arturo Bronson, Ph.D.

Kenneth Fishman, Ph.D.

Charles H. Ambler, Ph.D.
Dean of the Graduate School

# Dedication

I dedicate this thesis to my parents, Eleuterio Cabrera and Dora Madrid, and my brother, Tello Cabrera. Their continuous support, love, and communication motivated me to dedicate effort, time, and sacrifice to my thesis work.

# ASSESSING CORROSIVITY OF GALVANIZED SOIL REINFORCEMENTS FROM ELECTROCHEMICAL TESTS

by

DIANA ALEJANDRA CABRERA, BSCE, EIT

THESIS

Presented to the Faculty of the Graduate School of

The University of Texas at El Paso

in Partial Fulfillment

of the Requirements

for the Degree of

MASTER OF SCIENCE

Department of Civil Engineering

THE UNIVERSITY OF TEXAS AT EL PASO

August 2018

# Acknowledgements

I would first like to thank my thesis co-chair Dr. Soheil Nazarian. The door to Dr. Nazarian office was always open whenever I needed help with my thesis work or when I had questions about my research and writing. He continuously helped me on steering me in the right direction on my thesis and research work. I would also like to thank my thesis co-chair Dr. Shane Walker for his constant support and advice on all stages of my research work. I also thank Dr. Arturo Bronson and Kenneth Fishman who gave me valuable input and helped me understand many topics related to my thesis, and for being part of my thesis committee. In addition, I would like to acknowledge staff members, Jose Garibay, Sergio Rocha, and Dr. Imad Abdallah, which worked closely with me. I value their time, help, and involvement directly related to my research work and skills.

I must express my very profound gratitude to my friends, Isaac Aguilar, Melissa Escalante, Stephanie Acuña, Alejandra Escajeda, Jose Luis Arciniega, and Luis Alberto Lemus, which offered me their time, continuous encouragement, and words at all times. I would like to thank my coworkers and colleagues at CTIS, especially Luisa Morales and Matthew Gonzalez. I would also like to thank Yadira Calderas for working closely with me and helping me on my thesis process.

Finally, I would like to acknowledge the most important persons in my life. Thanks to my parents, Eleuterio Cabrera and Dora Madrid, I learned the value of education, hard work, and dedication. Thanks to my brother, Tello Cabrera, I learned to stay strong during my thesis and master's program. I am deeply thanked for their unconditional love and believing in me when I could not. This accomplishment would not have been possible without their unfailing support. Thank you all.

# Abstract

The accurate estimation of the service lives of mechanically stabilized earth (MSE) walls requires a proper evaluation of the corrosion potential through electrochemical test methods. Robust field tests are required to assess the corrosivity of galvanized metal used in MSE walls. To simulate an environment similar to an MSE wall, cylindrical soil specimens about 12 in. (300 mm) in diameter and 10 in. (250 mm) in height were constructed. For every specimen, two instruments were used. The first instrument measured the polarization resistance corrosion tests carried out on galvanized strips and meshes, as well as epoxy-coated rebars. The second instrument measured the soil resistivity of the specimen. Tests were conducted at moist and wet (submerged) states on materials that exhibited high, medium, and low resistivity values. A coarse and a fine aggregate gradation were considered to study the impact of the grain size distribution on the corrosivity. Five analytical models were prepared to estimate the rate of corrosion using the corrosion tests. Cumulative corrosion was measured on sacrificial coupons using SEM and an electronic thickness gauge. Test results confirmed that materials with high resistivity exhibit low corrosion rate. Fine-grained backfill displayed higher corrosion rates due to their high fines content.

# Table of Contents

# List of Tables

# List of Figures

# Chapter 1: Introduction

Mechanically stabilized earth (MSE) walls have become increasingly popular. Beckham et al. *(2013*) reported that 33 of 41 highway agencies in US and Canada that responded to their survey use galvanized steel as their MSE walls reinforcement. MSE walls have been used in Texas since the late 1970s (*Briaud et al., 2017)*. From 2010 to 2011, the Texas Department of Transportation (TxDOT) reported that 72% of the retaining walls in Texas were MSE walls (*Galvan, 2011*). Although known for their ease of installation and relatively rapid construction, the service life of MSE walls is affected by several factors. The corrosion of the reinforcements inside the MSE wall is one of the most critical factors. A number of nondestructive methods are available for estimating the corrosion rate of the metallic reinforcement. Most of these methods require the use of an experienced technician to perform them properly and significant engineering judgment by the analyst to estimate the rate of corrosion. As such, it is not uncommon that several analyst using the same field data may arrive at different rates of corrosion. The purpose of this study consists of evaluating and assessing the rate of corrosion of MSE wall reinforcements and propose a protocol to estimate the rate of corrosion accurately and systematically.

## 1.1 BACKGROUND

An MSE wall is composed of alternating layers of reinforcement and compacted backfill behind a facing element to hold a structure that restrains lateral forces (*Alzamora, 2009*). Metallic materials, mainly galvanized steel or welded wire mesh, have been widely used as MSE wall reinforcement (*Anderson et al., 2012*). Both welded wire mesh and ribbed strips undergo hot-dip galvanization by submerging steel (e.g., type A36 or A709) in the form of mesh or strip into a molten zinc bath. The final product should comply with a coating thickness prescribed in ASTM

A123 or ASTM A641. Gladstone et al. (*2006*) indicated that the zinc losses from galvanized metals used in MSE walls was typically 15 μm/yr (0.6 mpy) for the first two years, and 1 μm/yr (0.04 mpy) after that. The American Association of State Highway and Transportation Officials (AASHTO) recommends a minimum zinc coating thickness of 86 μm (3.4 mils) for galvanized reinforcements.

Table 1.1 presents the Federal Highway Administration (FHWA) backfill gradation and electrochemical requirements for MSE walls (*Berg et al., 2009*).

Table 1.1 FHWA backfill gradation and electrochemical requirements (from Berg et al., 2009)

| Backfill Gradation Requirements | | Electrochemical Requirements | |
|---|---|---|---|
| Sieve Size | Percent Retained, % | Characteristic | Requirement |
| 4” | 0 | pH | 5.0 to 10.0 |
| #40 | 40-100 | Resistivity, min. | 3000 ohms-cm |
| #200 | 85-100 | Chlorides, max. | 100 ppm |
| - | - | Sulfate, max. | 200 ppm |

Table 1.2 presents the four backfill gradations and the electrochemical requirements for MSE walls as specified in TxDOT Item 423. Type AS contains minimal amount of fine aggregates and high amount of coarse aggregates, while Type BS contains more fine content and less coarse aggregates. Type CS and DS are composed of rock backfill.

Table 1.2 TxDOT Item 423 backfill gradation and electrochemical requirements

| Backfill Gradation Requirements | | | Electrochemical Requirements | |
|---|---|---|---|---|
| Type | Sieve Size | Percent Retained, % | Characteristic | Requirement |
| AS | 3” | 0 | pH | 5.5 to 10.0 |
| | 1/2” | 50-100 | | |
| | #4 | See Note | | |
| | #40 | 85-100 | Resistivity, min. | 3000 ohms-cm |
| | #200 | 95-100 | | |
| BS | 3" | 0 | | |
| | #4 | See Note* | | |
| | #40 | 40-100 | Chlorides, max. | 100 ppm |
| | #200 | 85-100 | | |
| CS | 3" | 0 | | |
| | #4 | See Note* | | |
| | #200 | 75-100 | Sulfate, max. | 200 ppm |
| DS | 3” | 0 | | |
| | 3/8” | 85-100 | | |
| | #200 | 95-100 | | |

*No. 4 sieve for determination of rock backfill as described in TxDOT Item 423

## 1.2 CURRENT PRACTICE

### 1.2.1 Resistivity Test Methods

Elias et al. (*2009*) indicated that the assessment of the corrosion potential was tied with proper evaluation of the electrical resistivity. Resistivity can be approximated with Equation 1.

$$\rho = RA/l \tag{1}$$

where ρ is the electrical resistivity of the soil (in ohms-cm), $R$ is the electrical resistance between two electrodes (in ohms), $A$ is the cross sectional area between the electrodes (in $cm^2$), and $l$ is the spacing between the electrodes (in cm). Equation 1 applies to certain resistivity test protocols, which are those performed with a soil resistivity test box.

The resistivity test protocols vary among agencies. AASHTO T-288 protocol is the recommended by FHWA to determine the minimum resistivity of a soil, and the most common among highway agencies. The protocol for this test consists of obtaining about 1.5 kg (3.3 lb) dried sample of backfill passing #10 sieve, mixing it with 150 mL (0.3 lb) of distilled water,

covering it, and allowing it to stabilize for 12 hrs. Then, the geomaterial is compacted in a box with nominal inside dimensions of 100 mm x 150 mm x 45 mm (4 in. x 6 in. x 1.75 in.). To calculate the resistivity of the geomaterial as per Eq. 1, the electrical resistance of the geomaterial is measured by passing a constant alternating current voltage through two plate electrodes secured to opposite faces of the box. After recording the resistance, the sample is mixed with another increment of distilled water, placed in the box, and a new resistance is recorded. The previous step is repeated until the minimum resistivity is reached. TxDOT test method, designated as Tex-129-E, is similar to AASHTO T-288. However, the nominal sample dry weight is about 1.3 kg (2.9 lb) passing the No. 8 sieve without stabilization period. In comparison to AASHTO-T288, Tex-129-E test is terminated when a minimum resistivity is obtained or once the sample reaches 100% saturation.

Borrok et al. (*2013*) studied the effectiveness of Tex-129-E test protocol in assessing the performance of coarse backfills. They found that the minimal amount of aggregates passing No. 8 sieve that was contained in the coarse backfills negatively impacted the representativeness of electrochemical properties obtained in the lab. In order to accommodate coarse backfill samples with more representative gradations, two additional boxes with the dimensions doubled and quadrupled in relation to the original box size were recommended by Arciniega (*2017*).

### 1.2.2 Corrosion Rate Estimation Methods

The electrochemical galvanic corrosion tests are classified into the following three categories (*Baboian, 1995*):

1. Sensitive galvanic current measurement (ASTM G71). This measurement involves an ordinary galvanic couple that consists of two dissimilar metals in contact with a corrosive electrolyte. Once the galvanic couple is exposed to an electrolyte, very low

current between the dissimilar metals is forced to flow through an external wire. This current is measured with a zero-resistance ammeter or by voltage drop across a 1-ohm shunt resistor.

2. Galvanic series determination (ASTM G82). This measurement involves placing the selected metals from the galvanic couple individually in the environment of interest and monitoring their electrochemical potential with time. During galvanic series, the metal with higher electronegative potential is known as the anode and suffers accelerated corrosion when placed in a galvanic couple.
3. Polarization curve measurement. Polarization curves can be obtained galvano-statically, potentio-statically, or potentio-dynamically, where the latter is the most common. Galvano-static polarization curves, as per ASTM G97, are used to determine the efficiency of sacrificial anode materials (e.g. zinc, aluminum, and magnesium). Potentio-static and potentio-dynamic polarization curves are described in ASTM G5. Potentio-static polarization curves are obtained to predict the long-term galvanic corrosion performance by exposing individual specimens of each metal at a variety of different potentials until steady-state behavior is reached. Potentio-dynamic polarization curves are conducted at the slowest scan rate possible to predict long-term galvanic corrosion behavior.

Borrok et al. (*2013*) indicated that ASTM G5 did not provide sufficient accuracy for coated metals, such as galvanized reinforcements. Although ASTM G5 provides comprehensive information on characterizing the oxide layer on the metal, Borrok et al. recommended the use of electrochemical impedance spectroscopy (EIS), Tafel plots, and Linear Polarization Resistance

(LPR) for additional information on other reactions (e.g., zinc and zinc oxide layers) of galvanized carbon steel.

## 1.3 OBJECTIVES

This study focuses on two electrochemical parameters, which are corrosion rate and resistivity. The objectives of this study are the following items:

1. Produce a systematic data collection of Tafel and LPR tests and propose practices to analyze collected data in order to estimate the corrosion rate of galvanized reinforcements.
2. Obtain a relationship between the estimated (theoretical) corrosion rate, and other monitored parameters such as resistivity and conductivity.
3. Produce a systematic data collection of zinc thickness measurements of galvanized reinforcements and propose practices to analyze collected data in order to estimate the zinc thickness loss of galvanized reinforcements.
4. Select the practice that best correlates between the estimated zinc thickness loss (e.g. estimated cumulative corrosion) and the measured zinc thickness loss of galvanized reinforcements.

# Chapter 2: Literature Review

## 2.1 CORROSION ASPECT

### 2.1.1 Background

Corrosion is defined as the deterioration of a material due to chemical reactions with its environment (*Stansbury and Buchanan, 2000*). Some materials can resist corrosion naturally, and others are treated to avoid corrosion, such as galvanized metals (*Budinski, 2002*). The prevention and analysis of corrosion failures depend on recognizing the type of corrosion that can occur. According to Budinski (*2002*), the basic types of corrosion include uniform, pitting, crevice, stress cracking, intergranular attack, dealloying, erosion, and galvanic corrosion. The American Galvanizers Association (*AGA, 2018*) narrows down the corrosion types to pitting, microbial, high temperature, crevice, and galvanic corrosion. Pitting corrosion is known as localized and accelerated corrosion, which appears as small holes in certain areas of the metal. Microbial corrosion is caused by micro-organisms, such as sulfate-reducing bacteria, which produce hydrogen sulfide leading to sulfide stress cracking. High temperature corrosion consists of the deterioration of a metal due to a heating process. Crevice corrosion occurs on spaces where access to fluids from the environment is very limited, meaning that oxygen is restricted. Galvanic corrosion occurs when two different metals are in contact with an electrolyte (i.e., galvanic couple). In a galvanic couple, the more active or electro-negative metal, known as the anode, corrodes, while the more noble metal, which is the cathode, remains protected.

Galvanic corrosion occurs in an environment under an electrochemical cell. The set-up of an electrochemical cell experiment is shown in Figure 2.1. An electrochemical cell separates two half electrochemical reactions (i.e. oxidation and reduction half-reaction) corresponding to two

different electrodes (i.e. working and counter electrode) inside an electrolyte with an electronic exchange via an outer circuit (*Marcus, 2012*). The measurement of cell potentials, which is defined as the difference in potential across the electrodes of a cell, is the main aspect of the electrochemical cell experiment (*Bard, 1980*). One is mainly interested in measuring the potential of the oxidation half-reaction, which occurs at the working electrode, or anode. Potentials are measured with respect to a reference electrode. A reference electrode has a constant phase composition, which means that its potential is fixed. Any changes that occur on the electrochemical cell are directly attributed to the working electrode. When changes on the cell appear, the potential of the working electrode is observed or controlled with respect to the reference electrode. This also means observing or controlling the energy of the electrons within the working electrode (*Bard, 1980*).

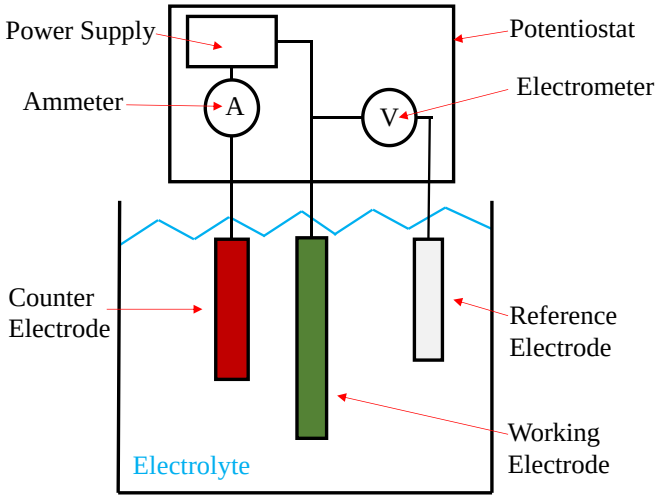


Figure 2.1 Electrochemical cell experiment

Changes in the electrochemical cell refer to changes in the half-reactions. Electrochemical equilibrium is reached when the anodic and cathodic partial reactions (i.e., the oxidation and reduction half-reaction, respectively) compensate each other, meaning that no reaction occurs. This process is known as the equilibrium potential $E_{eq}$, or Nernst potential. If the potential is

shifted positively with respect to $E_{eq}$, an anodic reaction will occur, and if the potential is shifted negatively with respect to $E_{eq}$, an overall cathodic reaction appears. The deviation of the electrode potential from $E_{eq}$ ($E - Eeq = \eta$) is called the overpotential, $\eta$ (*Marcus, 2012*). Both anodic and cathodic reactions change exponentially with the electrode potential, as described by the Butler-Volmer equation along with the Tafel equation. Techniques to measure these reactions using Tafel plots play a significant role in calculating corrosion rate.

An electrochemical cell experiment can be performed under potentio-static, galvano-static, and potentio-dynamic conditions. Potentio-static tests are conducted with a constant potential and measure current, while the galvano-static tests have constant current and measure potential. The most common experiment condition is the potentio-dynamic, or, potentio-dynamic polarization. During potentio-dynamic polarization, the electrode potential is varied at a specific rate by applying a very low current through the electrolyte. Potentio-dynamic tests use the principle of polarization to accelerate the corrosion process. The widely known potentio-dynamic polarization technique is the Linear Polarization Resistance (LPR), which is a measurement performed by scanning through a small potential range (±10 mV) between the counter electrode and the working electrode in the proximity to the open circuit potential ($E_{oc}$). Parameter $E_{oc}$ is the measured voltage that exists between the working electrode and the reference electrode under stable conditions.

### 2.1.2 Electrode Kinetics and Techniques Overview

To select the best practice of measuring corrosion rate, the electrode kinetics of electrochemical tests are studied. The electrode kinetics are described according to the electrochemical cell condition. For potentio-static conditions, the following equation known as the Butler-Volmer equation (*Butler, 1924, Volmer, 1930*) is applied:

$$i = i_o(e^{-\frac{\alpha_A nF\eta}{RT}} - e^{-\frac{\alpha_C nF\eta}{RT}}) \quad (2)$$

where $i$ is current density (in amps/cm$^2$), $i_o$ is exchange current density (in amps/cm$^2$), $\alpha_A$ is the anodic charge transfer coefficient, $\alpha_C$ is the cathodic charge transfer coefficient, $n$ is the number of electons involved in the electrode reaction, $F$ is the Faraday constant, $R$ is the universal gas constant, $T$ is absolute temperature (in K), and $\eta$ is overpotential ($E - Eeq = \eta$, in volts).

The Butler-Volmer equation, which measures total current density, has two limiting cases depending on the overpotential region. At high overpotential regions, the total current density is determined from a simplified version of the Butler-Volmer equation, called Tafel equation and plot. The Tafel equation measures the anodic (Equation 3a) and cathodic (Equation 3b) reactions at high overpotentials (*Jones, 1992*):

$$\eta_A = \beta_A log \frac{i_A}{i_0} \quad (3a)$$

$$\eta_C = \beta_C log \frac{i_C}{i_0} \quad (3b)$$

where $\eta_A$ and $\eta_C$ are anodic and cathodic overpotential, respectively (in volts), $\beta_A$ and $\beta_C$ are the Tafel constants for the anodic and cathodic half reaction (in volts/log cycle of current), $i_A$ and $i_C$ are the anodic and cathodic current densities, and $i_o$ is the exchange current density (in amps/cm$^2$).

Stern and Geary (*1957*) and Oldham and Mansfeld (*1971*) presented the polarization technique, LPR, as an alternative to the Tafel plot. After conducting an LPR measurement, the resulting scanned current is plotted versus potential to acquire the slope $\Delta V/\Delta I$ (Figure 2.2a). The corrosion current is related to the slope of the plot as:

$$i_{corr} = \frac{\beta_A \beta_C}{2.303\frac{\Delta V}{\Delta I}(\beta_A + \beta_C)} \quad (4)$$

where $i_{corr}$ is the corrosion current (in amps), $\beta_A$ is the anodic slope of Tafel plot (in volts/log cycle of current) and $\beta_C$ is the cathodic slope of Tafel plot (in volts/log cycle of current). The Tafel

slopes are usually assumed in the LPR equation. As reviewed by Jones (*1992*), the Tafel slopes can be obtained by extrapolating the two linear portions of a logarithmic current versus potential plot until the two lines intersect (Figure 2.2b). The two linear portions consist of the anodic reaction current and the cathodic reaction current among the working electrode and the counter electrode metals and the electrolyte. After obtaining the Tafel slopes, Equation 4 is rearranged to:

$$R_p = \frac{\Delta V}{\Delta I} = \frac{\beta_A \beta_C}{2.303 i_{corr}(\beta_A + \beta_C)} \tag{5}$$

where $R_p$ is polarization resistance (in ohms).

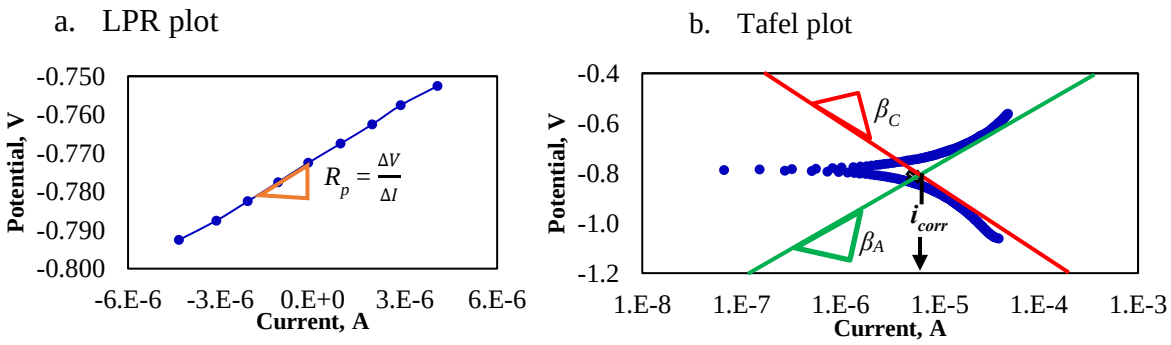


Figure 2.2 Stern and Geary (1957) technique

At low overpotential regions, the total current density is determined from another version of the Butler-Volmer equation proposed by Bard and Faulkner (*2001*) in the form of:

$$i = \frac{RT}{nFR_p} \tag{6}$$

where $i$ is corrosion current or corrosion current density(in amps or amps/cm$^2$), $R$ is the gas constant, $F$ is the Faraday's constant, and $T$ is temperature. Equation 6 is essentially the Butler-Volmer equation linearized with the first term of a McLaurin series, used to calculate the total current density at low overpotential regions. Bard and Faulkner found that an electrochemical cell experiment always lead to a multi-electron transfer reaction (i.e. zinc oxidation of the galvanized

coating). Therefore, Equation 6 is used for multi-electron transfer reactions ($n \geq 2$). Equation 6 is a polarization technique that applies for potentiostatic and potentiodynamic conditions. Once $i_{corr}$ or $i$ is determined from any of the previous techniques, corrosion rate is calculated.

Based on Faraday's Law, corrosion rate is estimated from $i_{corr}$ or $i$ as seen in Equation 7 (*Jones, 1992*):

$$CR = (3.27x10^6)\frac{i_{corr}W}{\rho n} \tag{7}$$

where $CR$ is corrosion rate (in μm/yr), $W$ is the atomic weight (e.g., 65.37 for zinc), ρ is the density (e.g., 7.14 g/cm$^3$ for zinc), and $n$ is the valence (e.g., 2 for zinc).

### 2.1.3 Corrosion Characterization

#### *2.1.3.1 Scanning Electron Microscope (SEM)*

The galvanized coating protects the metal when the zinc and atmospheric compounds like $0_2$, $H_20$ and $CO_2$ react. When these reactions occur, a thin film, which is highly insoluble in water, adheres to the metal's surface and generates a barrier that isolates zinc from the aggressive environment (*Pistofidis, et al., 2005*). The microstructure of zinc coatings or galvanized coatings is studied metallurgically to provide information on the corrosion protection. Scanning Electron Microscope (SEM) is implemented to observe the zinc layer thickness, which ultimately predicts the corrosion protection. The SEM scans images at high spatial resolution and in a low acceleration voltage area (*Todokoro and Ezumi, 1996*). The process consists on obtaining a cross-section of reinforcement, then polish it with SiC grit paper, and finally polish it with alumina particles (*Borrok et al., 2013*). After the sample is prepared, the samples are ready for SEM imaging. In addition to zinc thickness measurement, SEM also provides information on the metallurgical phases at the zinc layer.

#### *2.1.3.2 Coating Thickness Probe*

The zinc coating thickness is measured nondestructively with a dry film thickness gauge or probe. Dry Film Thickness (DFT) is defined as the thickness of a coating as measured above the substrate (*Corrosionpedia, 2018*). Dry film gauges work under the magnetic induction process. Magnetic induction consists of an excitation current that generates a low-frequency magnetic field with a strength that corresponds to the distance between the probe and the base material, or steel (*Fischer, 2018*). The standard test method to measure zinc thickness with a dry film thickness gauge is described in ASTM B 499. Before performing zinc thickness readings, the gauge must be calibrated and adjusted according to the manufacturer's specifications. After calibrating the gauge, a series of measurements are recorded; for each measurement, five readings are taken, removing the probe after each reading, and then, readings are averaged. The readings can be affected by factors such as the surface cleanliness, the probe orientation, and the pressure applied to the probe. Therefore, after recording three readings, if two out of the three readings differ from each other by more than 5% of the average reading or 2 $\mu$m (0.08 mil), whichever is the greater, then the measurement is discarded and repeated.

### 2.1.4 Case Studies

Elias et al. (*2009*) gathered guidelines and research findings from three previous FHWA manuals to present a standard reference for highway projects involving reinforced soil structures. Elias et al. (*2009*) provide feedback on common galvanized coatings used in industry including GALFAN (Zn-5% aluminum-mischmetal alloy), Dunois (85% Zn-15%Al thermal spray), and hot-dip galvanized metals. The latter continues to be the most common. Another type of reinforcement, which are the fusion-bonded epoxy coatings, are dielectric, therefore cannot conduct current, which ultimately terminates the corrosion process. A study by the South Dakota

Department of Transportation (SDDOT, *2005*) observed the effectiveness of different reinforcements by measuring half-cell potentials. Monitored MSE walls in South Dakota had three types of reinforcements. The black steel straps exhibited the most aggressive corrosion, while galvanized steel straps had relatively low corrosion and zinc reaction product. Epoxy coated straps exhibited no evidence of active steel corrosion (*Johnston, 2005*).

Borrok et al. (*2013*) studied the impact of coarse backfill materials at different moisture conditions in traditional electrochemical test methods. Borrok et al. estimated the corrosion rate by performing EIS. They also provided information about the iron oxide layer and zinc oxide layer, and the solution resistance of the thin film electrolyte on the zinc surface. They constructed specimens that contained resistivity probes, a piece of reinforcement, and a corrosion coupon that resembled a corrosion cell. The electrochemical techniques used to assess the corrosion of galvanized steel were divided into: 1) long-term monitoring for integrity of galvanized carbon steel 2) mechanistic determination of corrosivity of Zn/Fe couple, and 3) rapid determination of corrosivity of Zn/Fe couple. Polarization curves for four solutions (0.0001 M NaCl solution, 0.001 M NaCl solution, 0.01 M NaCl solution, and 0.1 M NaCl solution) were conducted to estimate their corrosion rates. Corrosion rate that decreased with decreasing the molarity were in the range of 31 μm/yr (1.2 mpy) for 0.1 NaCL M to 0.04 μm/yr (< 0.1 mpy) for 0.1 NaCl M. For the embedded coupons, the first year of monitoring predicted about 15 μm/yr (0.6 mpy), which agreed with Elias (*2009*) model of the first two years loss; however, after the first year, the corrosion rate plateaued to 7 μm/yr (0.3 mpy). The SEM results indicated that Zn layer thickness varied from 74 μm to 124 μm (3 mil to 5 mil). Gladstone et al. (*2006*) reported half-cell potential and zinc thickness readings on sacrificial galvanized steel coupons. They found that it would take around 30 years or more for zinc to be consumed in backfills, which complied with the AASHTO design.

Beckham et al. (*2005*) instrumented four MSE walls and obtained corrosion rates via LPR. No visible corrosion was observed from sacrificial galvanized strips that had service lives of more than 20 years. Measured corrosion rates were much less than the maximum corrosion rates assumed in the design. The free corrosion potential was also monitored on the four MSE Walls. The corrosion potential is defined as the voltage of a reinforcement element of interest measured with respect to a suitable reference electrode (*Elias et al., 2009*). The change of free corrosion potential with time indicated that corrosion was occurring on the monitored walls. Therefore, if readings of the free corrosion potential of galvanized reinforcing elements became less negative with time, corrosion was spreading. Beckham et al. found that the analyzed free corrosion potential values were comparable to the typical values for two of the four tested walls.

Raeburn et al. (*2008*) discussed the destructive and nondestructive methods of corrosion monitoring. They recommended to filter out the ohmic resistance for a more robust polarization resistance measurement, since the ohmic resistance is related to the resistance of the soil. Gladstone et al. *(2006*) recommended to obtain corrosion rate readings throughout the year, to ultimately attain an average corrosion rate for the structure. Berke and Sagüés (*2009*) investigated the results of monitoring done by the Florida Department of Transportation (FDOT) at nine MSE structures. LPR measurements, macro-cell current measurements, and direct metallographic examination were performed on plain steel and galvanized reinforcements. Corrosion rates for the embedded plain steel elements were around 0.6 μm/yr (0.02 mpy), and for the galvanized steel elements less than 1 μm/yr (0.04 mpy). The galvanized layer from sacrificial coupons was moderately damaged, and corrosion rates ranged in the 0.2 to 1.1 μm/yr (0.01-0.4 mpy) range. After collecting LPR measurements and estimating corrosion rates, Berke and Sagüés developed a statistical model. The model was created to project the evolution of corrosion related damage in

a generic Florida MSE wall by considering the estimated corrosion rates from Berke and Sagüés study and data from previous surveys.

## 2.2 RESISTIVITY ASPECT

Since soil resistivity governs the ionic current pathway, it has a strong influence on corrosion rate. Corrosion of MSE reinforcements increases as resistivity decreases (*King, 1977*). However, if resistivity is high, localized rather than general corrosion may occur. To analyze backfill resistivity, Borrok et al. (*2013*) prepared specimens under three moisture contents of wet and dry, always wet, and always dry. A data logging program continually measured the resistivity. The results for the dry condition showed that resistivity gradually increased; while, at wet condition, resistivity remained relatively constant, and at wet and dry condition, resistivity cycles of increases and decreases appeared.

Arciniega (*2017*) demonstrated that the Tex-129-E traditional resistivity method is not representative of coarse materials. To accommodate such issue, resistivity boxes with dimensions that were double (2X) and quadruple (4X) of the original resistivity box were constructed. Tests were conducted on fines, fine sand, coarse sand, and gravel fractions of each material in addition to three TxDOT gradations for MSE walls (Type BS, AS, and DS). The two additional boxes (2X and 4X) accommodated the testing for coarse aggregates through a modified version of Tex-129-E. For all gradations, the resistivity decreased with an increase in moisture content. Type BS (fine-grained) materials had the lowest resistivity that were similar to those of the Tex-129-E method. At the same time, Type DS (coarsest of the three gradations) materials had the highest resistivity. In a given backfill material, the coarse portion exhibited a higher resistivity than the portion passing the No. 8 sieve. Arciniega (*2018*) developed a model that predicts the resistivity of a backfill material as a function of its composition as a weight fraction of the constituents. For

his master's thesis, Arciniega developed another model that predicts the resistivity of an aggregate based on moisture conditions and minimum resistivity.

## 2.3 OTHER ASPECTS

Elias et al. (*2009*) discussed that corrosion is dependent on the following factors: water content, soil resistivity, pH, chloride content and sulfate content. In addition, the level of compaction and grain size distribution of backfill placed around reinforcement impact the rate of corrosion. If the moisture content is greater than 25-40%, the rate of general corrosion will increase (*Elias, 2009*). Sokolic et al. (*2015*) found that resistivity rapidly decreases with an increase in moisture content on sands. As water content increased from 0% to 40%, the resistivity of two types of sands decreased from 600 kohms-cm to approximately 80 kohms-cm, and for two other sands, the resistivity decreased from 550 kohms-cm to approximately 40 kohms-cm (*Sokolic et al., 2015*).

Soriano and Alfantazi (*2015*) studied the impact of organic compounds on galvanized steel. The contact of galvanized metal with solutions of citric acid, oxalic acid, humic acid and dextrose was investigated. Each solution was prepared at four different concentrations: 0.10 wt%, 0.25% wt., 0.50% wt., and 1.00% wt. Metals in contact with citric acid produced the highest current densities, therefore the highest corrosion rates. Soriano and Alfantazi observed that the formation of a layer of zinc corrosion products and possibly zinc-organic complexes on the surface of galvanized steel in an environment with a minimal amount of oxalic acid (concentration of 0.10 wt. %) would protect the material from further corrosion by acting as physical barrier. In addition, all their solutions exhibited conductivity that increased as a function of the solution concentration.

Thornley and Siddharthan (*2010*) compared the conductivity as per Nevada T235B test method and resistivity as per AASHTO T-288 of backfills of Nevada Department of

Transportation (NDOT). They concluded that the Nevada T235B test method was not conservative with respect to identifying aggressive soils.

# Chapter 3: Methodology for Estimating Corrosion Rates of Galvanized Strips

## 3.1 Introduction

Figure 3.1 shows the plan followed to achieve a systematic method to estimate the corrosion rate of galvanized reinforcements. The first stage was the implementation of an experimental procedure. The second stage corresponded to the analyses of the experimental data. Finally, the last stage was the overall discussion between methods to possibly decide on the "best" practice to estimate corrosion rate. A comparison between the analyzed current-voltage data and the cumulative corrosion measurements in a time relationship is desired to establish a robust protocol.

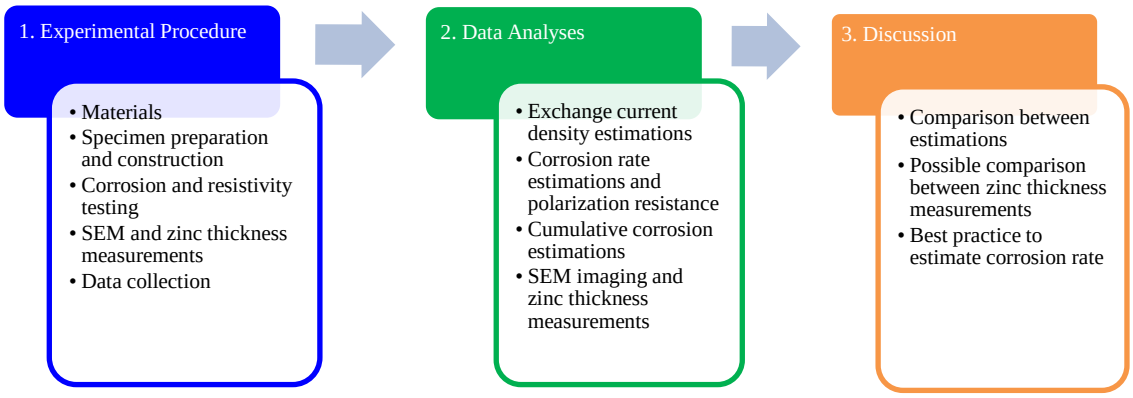


Figure 3.1 Methodology Diagram

## 3.2 Experimental Procedure

The experimental procedure consisted of conducting Tafel and LPR tests on metals embedded in cylindrical specimens resembling an MSE walls. Other parameters that were measured on the specimens were resistivity and conductivity. In addition, zinc thickness measurements were conducted on sacrificial coupons. The specimen preparation, tests, and data collection are described next.

### 3.2.1 Material Selection

Four representative backfill materials were selected based on the resistivity values obtained as per TxDOT Tex-129-E of about 20 materials tested as reported by Arciniega (*2017*). Figure 3.2 shows the representative particle size distributions used to fabricate a fine-grained (Type BS) and a coarse-grained backfill (Type AS) from all four materials. The specification limits are marked in Figure 3.2 as small circle and triangle symbols. In this study, the gradations that passed through the middle of the specification ranges were selected. The AS gradation limit is mainly characterized by 85% to 100% retained on the No. 40 sieve, therefore higher content of coarse aggregates. On the other hand, the BS gradation is limited by 85% to 100% retained in the No. 200 sieve, meaning that higher fine aggregates are present.

The four materials are presented in Table 3.1, ranked based on their minimum resistivity values. Material 1 has the highest resistivity, while Material 4 the lowest. In Arciniega's study (*2017*), all materials passed TxDOT resistivity limit, except for the BS gradation of Material 4. Since the density of the material affects its resistivity directly and corrosion rate indirectly, pre-determined density was maintained for each material and each gradation. Those densities, which are also reported in Table 3.1, were obtained from Arciniega (*2017*). Atterberg limits are shown in Table 3.2 only for the BS gradation of each material. Material 1 is nonplastic, while Material 2 is relatively nonplastic, due to its low bar linear shrinkage result. In contrast, Materials 3 and 4 are plastic and relatively plastic, respectively. The aggregate type is presented for all materials in Table 3.2.

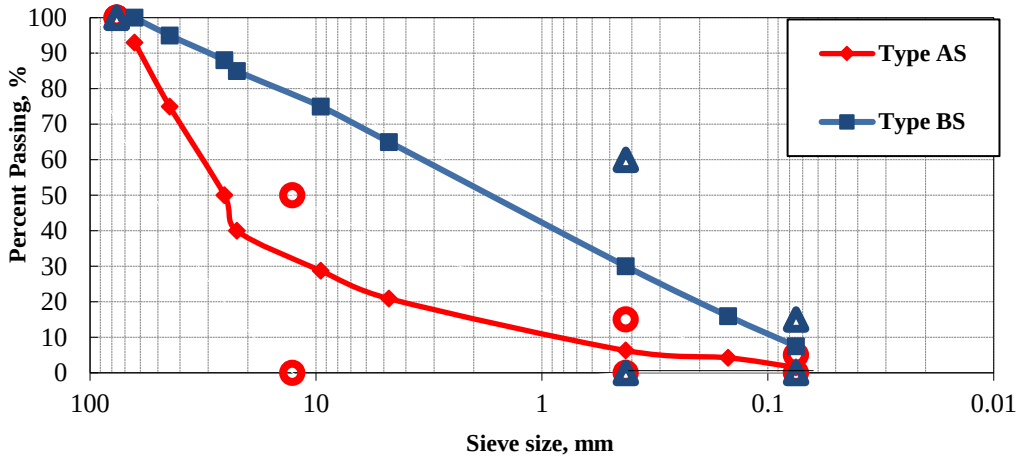


Figure 3.2 Cumulative grain distributions for Type AS and BS used in this study

Table 3.1 Resistivity and density for materials used (from Arciniega, 2017)

| Material | Resistivity (ohms-cm) | | Density (pcf) | |
|---|---|---|---|---|
| | AS | BS | AS | BS |
| 1 | 50673 | 25337 | 101 | 88 |
| 2 | 20803 | 10935 | 102 | 94 |
| 3 | 17336 | 5334 | 111 | 114 |
| 4 | 3467 | 2160 | 108 | 101 |

Table 3.2 Atterberg Limits and aggregate type for materials used (from Arciniega, 2017)

| Material | Atterberg Limits (Type BS Gradation) | | | Mineralogy |
|---|---|---|---|---|
| | Liquid Limit | Plastic Limit | Bar Linear Shrinkage | |
| 1 | Nonplastic | Nonplastic | Nonplastic | Sandstone |
| 2 | Nonplastic | Nonplastic | 4 | Limestone |
| 3 | 23 | 13 | 11 | Limestone |
| 4 | 15 | 9 | 7 | Limestone |

### 3.2.2 Specimen Preparation

#### *3.2.2.1 Preparation of Test Jigs*

To measure corrosion and resistivity, two jigs were constructed for each specimen. The corrosion jig (see Figures 3.3a and 3.3b) consists of a stainless steel rod (5 in. or 127 mm long, and 0.5 in. or 13 mm in diameter), a galvanized strip (2 in. or 51 mm wide, 5 in. or 127 mm long, and 0.2 in. or 5 mm thick), a galvanized mesh section (a "cross" measuring 2 in. or 51 mm wide, 5 in. or 127 mm long, and 0.3 in. or 8 mm in diameter), and an epoxy-coated rebar (5 in. or 127 mm long, and 1.1 in. or 28 mm in diameter) connected to two acrylic bases. These elements were separated by 2.5 in. (64 mm). All exposed regions outside of the established surface areas of the elements were covered with rubber coating. The geometry of the trapezoidal bases facilitated the arrangement of the jig inside the cylindrical specimens. After constructing the corrosion jigs, the zinc thickness was measured in sixteen points on each galvanized strip specimen using the *Elcometer 456 Coating Thickness Gauge*$^{TM}$.

The resistivity jig (see Figure 3.3c) consists of four copper tubes (4 in. or 102 mm long, and 0.3 in. or 8 mm in diameter) connected to two acrylic bases. The copper tubes acted as probes that measure the soil resistance in a specific area of the cylindrical specimen. To be consistent with the traditional soil laboratory resistance tests (i.e., Tex-129-E), two outer electrodes were subjected to a 97 Hz voltage.

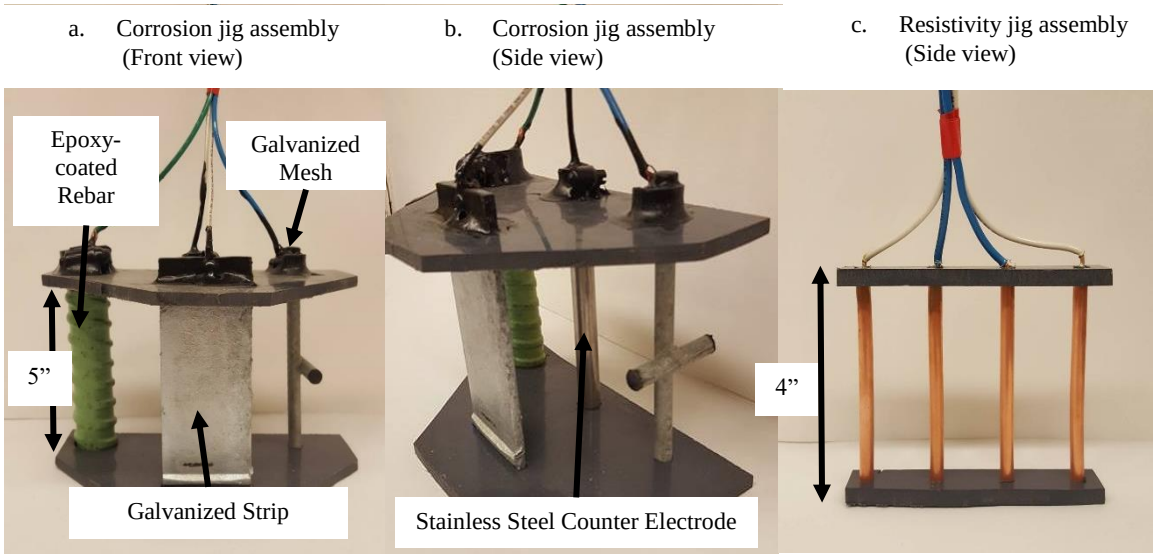


Figure 3.3 Corrosion and resistivity jigs

### *3.2.2.2 Specimen Construction*

The specimen construction pertained to the compaction of 16 cylindrical specimens where the corrosion and resistivity jigs were embedded. Four specimens (two gradations and two moisture contents) were prepared from each of the four materials. The two different moisture conditions were moist condition and wet condition. The specimens prepared at the moist condition were compacted with a 6% deionized (DI) water content, while the wet specimens were identified once a “sheen” of water was observed on the top surface of the compacted soil. The following procedure was followed to prepare the specimens in the moist condition (see Figure 3.4):

1. Dry, sieve and combine about 55 lb (25 kg) of the backfill to the relevant type AS or BS gradation.
2. Place the combined dry material from Item 1 in a concrete mixer and gradually add 3.3 lb (1.5 kg) of DI water. Mix for five minutes.
3. Place and manually compact one 2 in. (50 mm) thick soil layer to the specified density using a 12 lb (5.4 kg) weight.

4. Place the corrosion and resistivity jigs inside the bucket with the corrosion jig facing the resistivity jig with a separation of approximately 2 in. to 4 in. (50 mm to 100 mm).
5. Compact four additional 2 in. (50 mm) thick soil layers to the specified density using a 12 lb (5.4 kg) weight. Use a 4.4 lb (2 kg) weight to evenly distribute soil in areas near the jigs, which can be hard to compact with a larger weight.
6. Drill 0.2 in. (5 mm) holes at a height of 11 in. (280 mm) to bring the cables outside of the specimen. The specimen is sealed with its corresponding lid at all times.

The same procedure was followed for the wet specimens except that after Step 6, DI water was added at increments of 0.11 lb (50 mL) until the specimens reached nominal saturation (i.e., a sheen was observed).


Figure 3.4 Specimen preparation procedure

### 3.2.3 Zinc Thickness Measurements

After constructing the sixteen cylindrical specimens, three galvanized strip sacrificial coupons (2 in. or 51 mm wide, 2 in. or 51 mm long, and 0.2 in. or 5 mm thick) were embedded on each cylindrical specimen. Three sacrificial coupons were manually embedded or pushed on the last compacted layer of each specimen. The initial zinc thickness was measured in sixteen points on each sacrificial coupon using the *Elcometer 456 Coating Thickness Gauge*$^{TM}$.

After six months, one sacrificial coupon was exhumed from each cylindrical specimen. Scanning electron microscope (SEM) imaging was performed on a section of each exhumed sacrificial coupon. Figure 3.5 shows the procedure followed to prepare the coupon samples for SEM imaging. A section of each extruded sacrificial coupon is covered with epoxide resin and hardener for 7 hrs (Figure 3.5a). The coupons were then polished with four different sand mills (Figure 3.5b). After polishing, each coupon was mounted for imaging with a *Hitachi TM-1000* SEM (Figure 3.5c). The zinc thickness was observed at the entire length of one face of each coupon. The analysis was performed on *Microsoft Image Composer* software and *Digimizer* software.

a. Preparing the coupon b. Polishing the coupon c. Mounting the coupon on SEM


Figure 3.5 SEM procedure

### 3.2.4 Corrosion and Resistivity Testing

The corrosion (LPR and Tafel) testing with the *Gamry™ Framework* software was performed by scanning the voltage between the counter and working electrodes (see Figures 3.6a and 3.6b). The *Reference 600+* potentiostat manufactured by *Gamry* was selected to conduct Tafel and LPR tests. The galvanized mesh, galvanized strip, and the epoxy-coated rebar in the corrosion jig acted as working electrodes, while the stainless steel bar served as the counter electrode. A copper-copper (II) sulfate reference electrode with a porous tip saturated with $K_2SO_4$ was used to control the potential at the working electrode. The reference electrode porous tip was moistened with DI water and placed on the surface of the cylindrical specimen before a LPR or Tafel test was conducted. The reference electrode was embedded in an area close to the corrosion jig cables (see Figure 3.6a). For each element or working electrode in each specimen, LPR tests were completed weekly while one Tafel test was carried out monthly. Using the potentiostat software, the solution resistance was measured after conducting each LPR and Tafel test. The solution resistance was measured to adjust both LPR and Tafel analyses for the resistance produced by the corrosion current.

The resistivity measurements made with the resistivity jig (see Figure 3.6c) consisted of applying a 97-Hz voltage and measuring two voltage readings with a multimeter. The first voltage reading was taken from a 220 ohms resistor in the system and the second voltage reading from the two inner probes in the resistance jig embedded in the soil. Following Ohm's law, the first reading divided by the 220 ohms resistance is equal to the current in the system. The given current divided by the inner probes' voltage provided the resistance. Ultimately, this resistance was used to calculate the resistivity of the soil. Three soil resistance tests were repeated and an average from these was recorded weekly in conjunction with the corrosion measurements.

The electrical conductivity of the liquid associated with each wet specimen was also measured weekly with a *COM-100 HM Digital EC TDS & Temperature Waterproof Meter* device. The measurements were carried out by submerging the probes of the conductivity meter into the leachates extracted from the wet specimens.

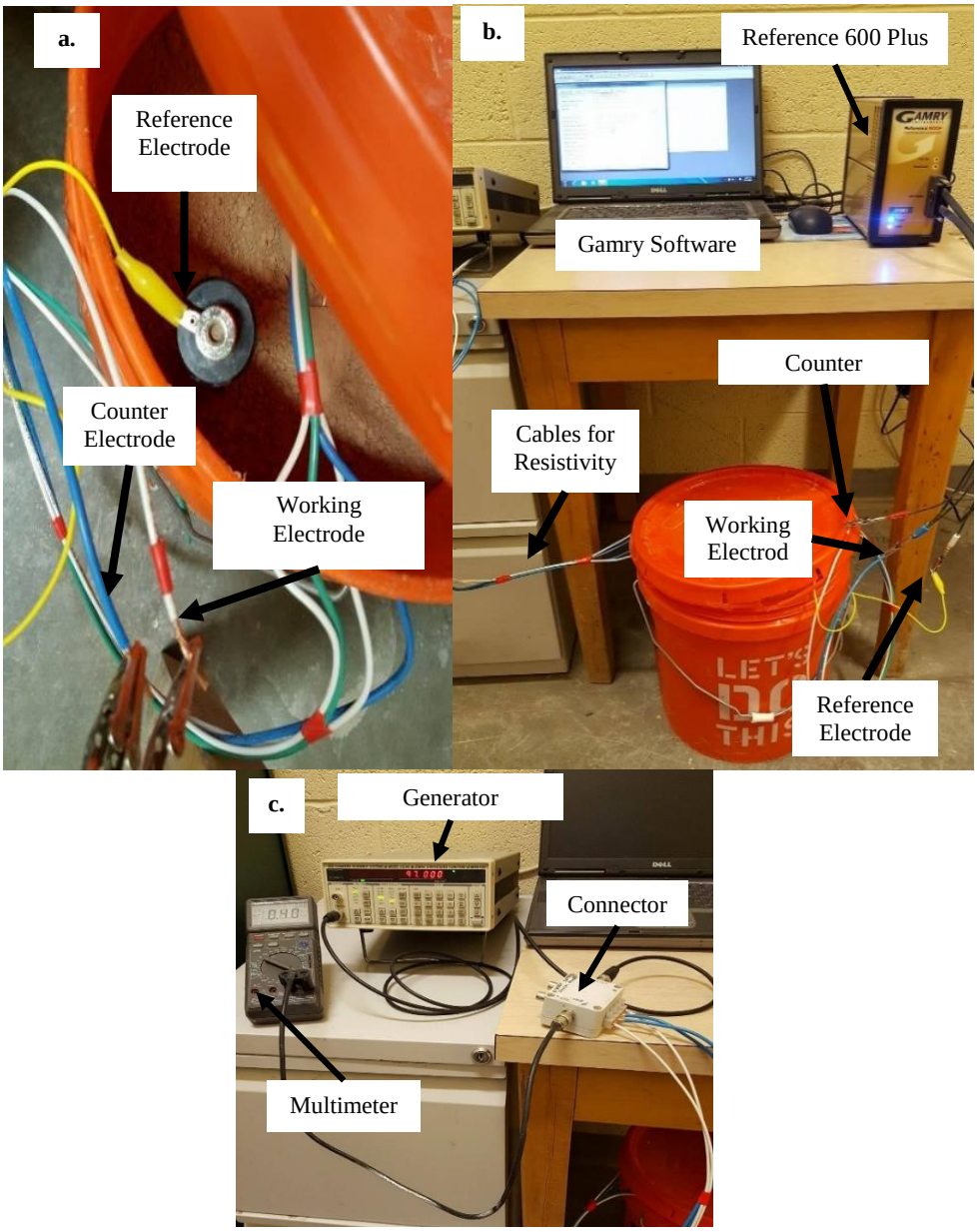


a. Electrode arrangement for LPR and Tafel measurement (Top view of specimen)
b. LPR and Tafel testing set-up
c. Resistivity testing set-up

Figure 3.6 LPR and resistivity testing

### 3.2.5 Collection of Corrosion Data

The current-voltage data was collected monthly in the form of Tafel tests and weekly in the form of LPR tests. The solution resistance and open circuit potential *Eoc* was collected for all tests. Table 3.3 presents the input parameters for the Tafel and LPR tests.

Table 3.3 *Gamry Framework* input parameters for Tafel and LPR tests

| Test | LPR | Tafel |
|---|---|---|
| Initial Potential (V) | -0.02 vs $E_{oc}$ | -0.4 vs. $E_{oc}$ |
| Final Potential (V) | +0.02 vs. $E_{oc}$ | +0.4 vs. $E_{oc}$ |
| Scan Rate (mV/s) | 0.333 | 1 |
| Working Electrode Area – Galvanized Mesh ($cm^2$) | 37.03 | |
| Working Electrode Area – Galvanized Strip ($cm^2$) | 117.74 | |
| Working Electrode Area – Epoxy-Coated Rebar ($cm^2$) | 202.71 | |

## 3.3 ALTERNATIVE CURRENT-VOLTAGE DATA ANALYSES

The alternative analyses of the current-voltage data entailed three steps. The first step consisted on estimating exchange-current density with different practices using the current-voltage data. Then, the corrosion rate, or rate of zinc thickness loss, was estimated. Finally, a numerical integration of the calculated corrosion rate, or discrete corrosion rate, was carried out to obtain an estimated zinc thickness loss or cumulative corrosion rate.

To estimate the exchange current density, the current-voltage data was changed to current density-voltage data. Current density is defined as the current within the corrosion cell in the absence of any external sources (*Fishman and Withiam, 2011*). To obtain current density, the current was divided by the working electrode area, leading to units of amps/$cm^2$. After changing the current-voltage data to current density- voltage data, five models to estimate exchange current density were created. Figure 3.7 shows a representation of each exchange current density model.

All exchange current density models, except Model 4, were observed at six overpotential windows of ±30 mV, ±50 mV, ±70 mV, ±90 mV, ±110 mV, and ±130 mV.

### 3.3.1 Tafel Models

#### *3.3.1.1 Traditional Tafel model*

Figure 3.7a represents how Model 1 is analyzed. Model 1 corresponds to the traditional Tafel extrapolation method. Model 1 estimates the Tafel slopes by obtaining two tangent slopes located at the linear portions of the anodic branch and the cathodic branch of the Tafel plot. The intercept of the two lines corresponding to the two slopes provided the open circuit potential, or $E_{oc}$. $E_{oc}$, which can be either negative or positive, is usually close to zero overpotential. The intercept is the estimated exchange current density of Model 1, called $i_{Tafel}$.

#### *3.3.1.2 Optimized Tafel model*

Figure 3.7b represents how Model 2 is analyzed. Model 2 is an optimized model based on the estimated $i_{Tafel}$ and the Butler-Volmer fit. The optimized exchange current density of Model 2 is called $i_{Optimized}$, and is restrained within a distance 1.0 to 1.3 from $i_{Tafel}$. Model 2 was analyzed to calculate the relative error of the Butler-Volmer fit. The Butler-Volmer fit consists of current density calculated using Equation 2.2 (x-values of fit) and potential using the original voltage data (y-values).

### 3.3.2 LPR Models

#### *3.3.2.1 Stern and Geary model*

Figure 3.7c represents how Model 3 is analyzed. Model 3 was calculated using the Stern and Geary formula (Equation 2.4) within a specified overpotential window of a LPR test. Model 3 is the traditional LPR estimation, therefore requires the estimated Tafel slopes. The Tafel slopes obtained from Model 1 are used for this purpose. The exchange current density from Model 3 is called $i_{LPR}$. As the overpotential window changes, the Tafel slopes remain the same, however $i_{LPR}$ changes. The range of y-axis in Model 3 is 2.5 times greater in order of magnitude than the y-axis of Tafel models (Model 1 and Model 2). The range of y-axis of Model 3 is displayed on a greater scale to clarify that LPR tests are ran in a low and short potential region, compared to Tafel tests, which require larger potential region.

#### *3.3.2.2 Bard and Faulkner model*

Figure 3.7d represents how Model 4 is analyzed. Model 4 was calculated using the Bard and Faulkner formula (Equation 2.6) at a ±10 mV overpotential window of a LPR test. Model 4 does not requires Tafel slopes. The exchange current density from Model 4 is called $i_{Bard\text{-}Faulkner}$. Model 4 uses LPR tests data, however it can also be analyzed using Tafel tests data (strictly at a ±10 mV overpotential window). The range of y-axis in Model 4 is 2.5 times greater in order of magnitude than the y-axis of Tafel models (Model 1 and Model 2). Again, the greater scale is provided to clarify that LPR tests are ran in a low and short potential region compared to Tafel tests.

### 3.3.3 Hybrid Model

Figure 3.7e represents how Model 5 is analyzed. Model 5 is similar to Model 3, because it uses the Stern-Geary formula (Equation 2.4) to estimate exchange current density. However, Model 5 calculates exchange current density using the Stern and Geary formula within a ±10 mV overpotential window from a Tafel test. Again, Tafel slopes are the estimated Tafel slopes from Model 1. The exchange current density from Model 5 is called $i_{Hybrid}$. The analysis for Model 5 is calculated at a ±10 mV overpotential window to assimilate a LPR region using a Tafel test. Model 5 relies on Tafel slopes, which are obtained from the results of the six overpotential windows of Model 1 (±30 mV, 50 mV, 70 mV, 90 mV, 110 mV, and 130 mV). This means that Model 5 always estimates exchange current density within a ±10 mV overpotential window from a Tafel test, but requires Tafel slopes (obtained from Model 1) that were not strictly calculated at the ±10 mV overpotential window.

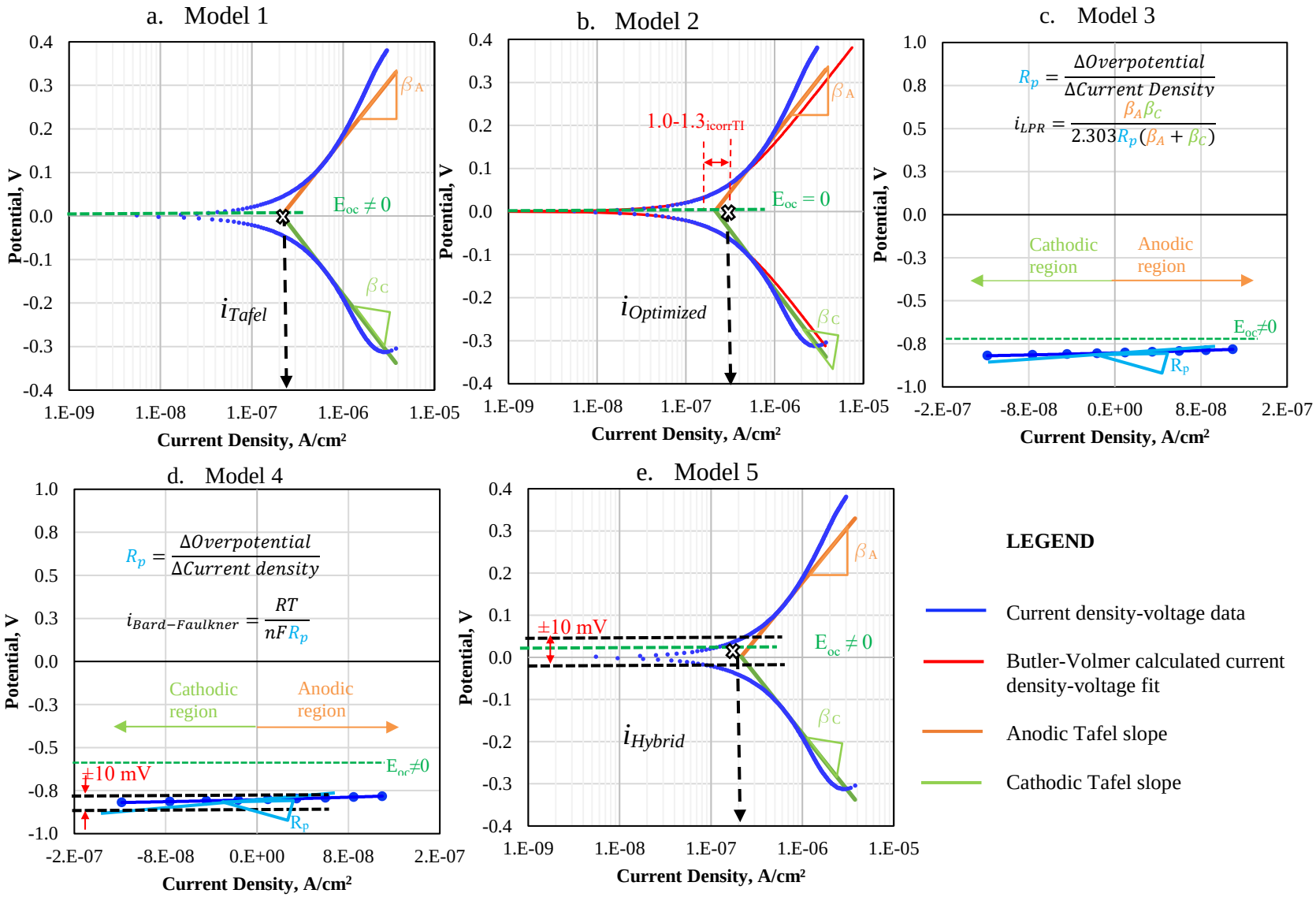


Figure 3.7 Representation of exchange current density models

# Chapter 4: Results and Discussion

## 4.1 Analyses Summary

The first twelve months of LPR data measured on the galvanized steel strips embedded in Material 4 moist specimens with AS and BS gradations are summarized in Figure 4.1. The range of corrosion current ($i_{corr}$) for the material with the BS gradation is ±20 µA, whereas the range for the material with the AS gradation is ±10 µA. The corrosion rate of these data is inversely proportional to the slope, which is known as the polarization resistance ($R_p$).

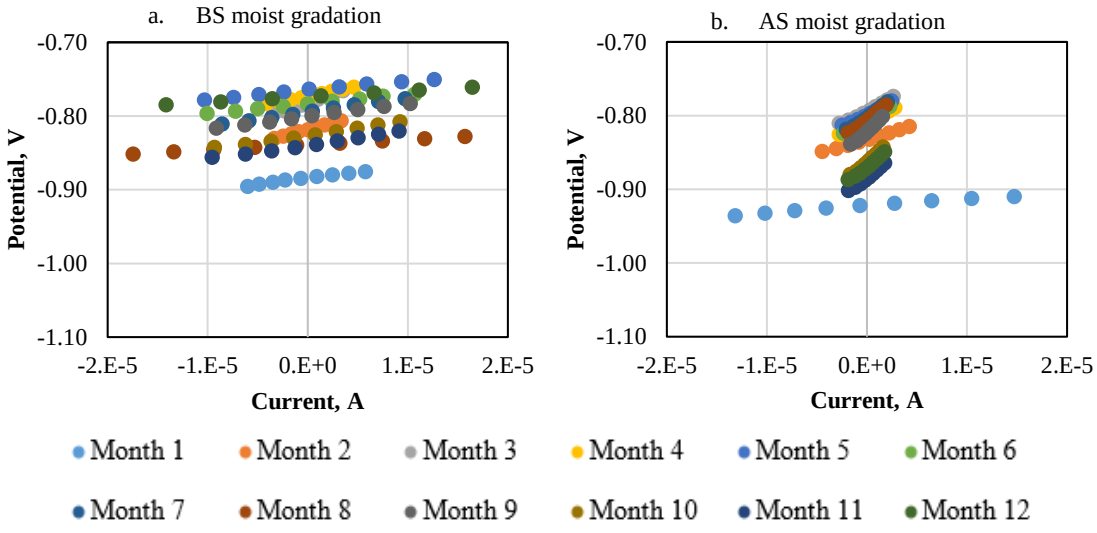


Figure 4.1 LPR tests from Material 4 moist specimens

The variations in $R_p$ from the galvanized steel strips with time for the moist and wet specimens made with Material 4 are displayed in Figure 4.2. The polarization resistance decreased with time for the Type BS wet sample (Figure 4.2b) and increased constantly for the wet Type AS sample (Figure 4.2d). The polarization resistance for Type BS moist sample (Figure 4.2a) increased during the first three months and then decreased. $R_p$ of the Type AS moist sample (Figure 4.2c) was considerably higher than the three other cases, yet $R_p$ for Type AS wet sample (Figure 4.2d) also constantly increased. Overall, the polarization resistance for the moist

specimens (Figures 4.2a and 4.2c) is two to three times greater than those for the two wet specimens, indicating higher rates of corrosion for the two specimens under wet condition (Figures 4.2b and 4.2d). The corrosion rates of the Type AS moist sample (Figure 4.2c) are the lowest (less than 0.2 µm/month or 2 µm/yr) and constantly decreased, while the corrosion rates of the Type AS wet specimen (Figure 4.2d) stabilized after Month 6 at approximately 0.3 µm/month or 4 µm/yr. For both specimens with Type BS gradation (Figure 4.2a and 4.2b), the corrosion rates fluctuated within the first six months. In addition, the corrosion rates of the wet specimens are higher in comparison to the corrosion rates of the moist specimens.

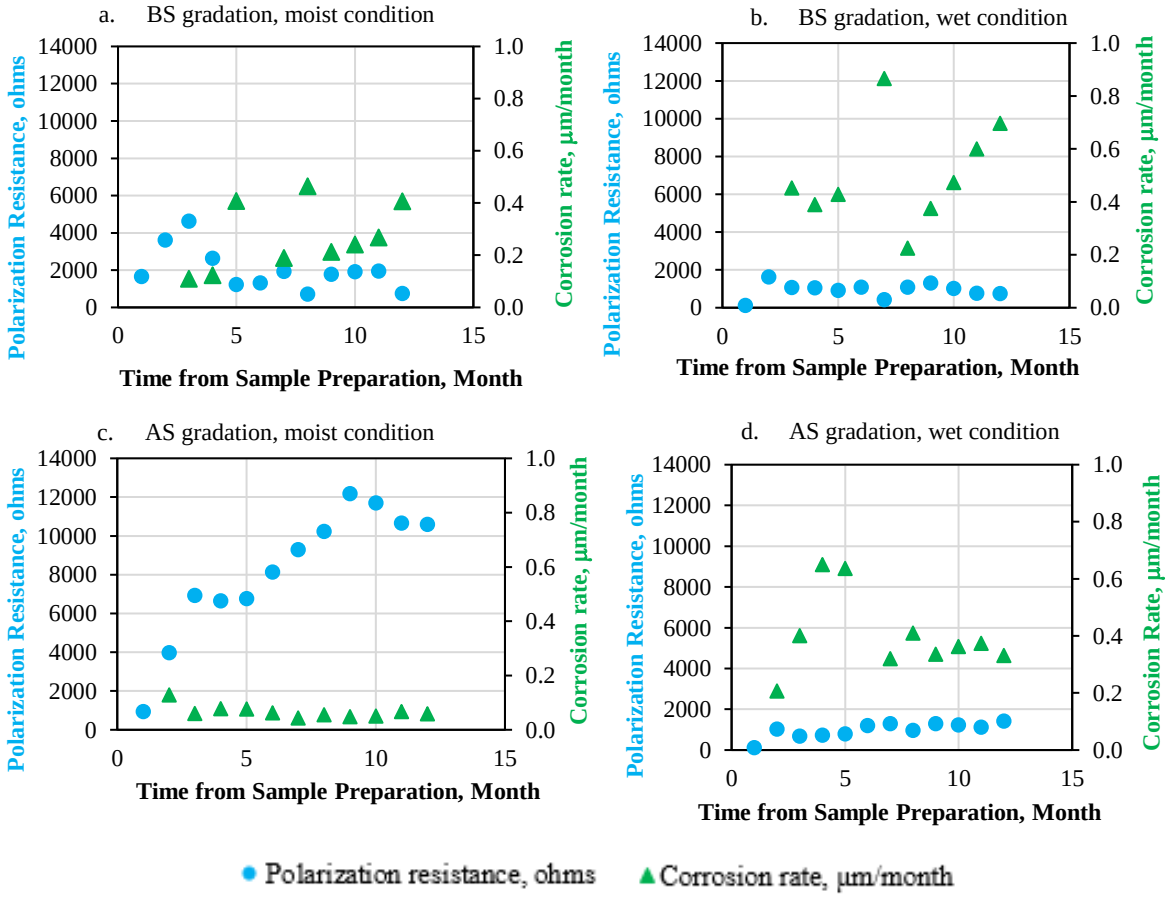


Figure 4.2 Polarization resistance and corrosion rate from Material 4 galvanized strips

The cumulative corrosion depth determined from the galvanized strips as a function gradation and moisture condition for all four materials are shown in Figure 4.3. The cumulative corrosion depth for the strips was calculated by numerically integrating the corrosion rate profiles shown in Figure 4.2 for all materials. The strips buried in Material 1, which corresponds to the backfill with the highest resistivity, show low corrosion (Figure 4.3a). Similarly, the strips buried in Material 2, which has high resistivity, exhibit low corrosion as well (Figures 4.3b). The strips placed in Material 3, which has low resistivity, exhibited the highest corrosion depth among the four materials (Figures 4.3c). Most of the strips under the wet conditions are corroding faster with time compared to the strips embedded in the moist backfills. The strips placed in Material 4, with the lowest measured resistivity, unexpectedly exhibit relatively low corrosion depths (Figures 4.3d). Overall, the corrosion depths are higher for the wet condition. In both moisture conditions, The Type BS specimens exhibit higher corrosion depths in comparison to the Type AS specimens.

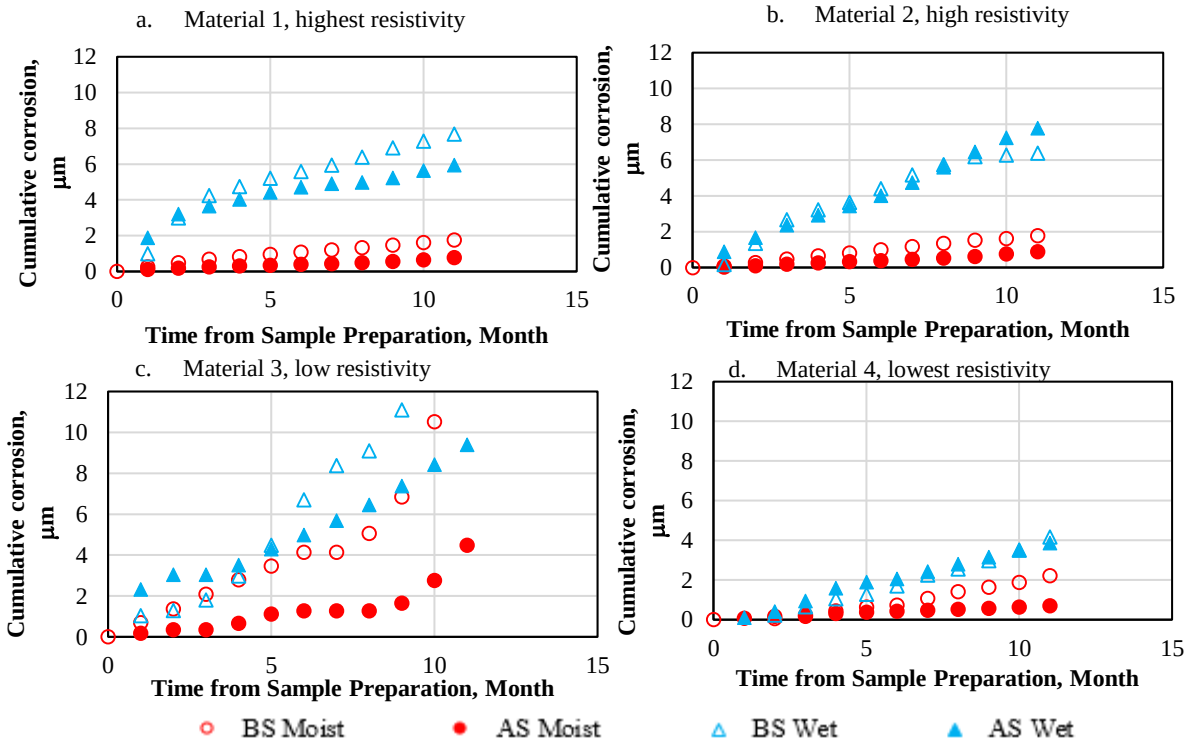


Figure 4.3 Monthly cumulative corrosion depths

The weekly backfill resistivity values measured with the embedded resistivity probes as a function of gradation and moisture condition for the four materials are shown in Figure 4.4. The resistivity values of the moist specimens for the most part follow the behavior that can explain the reported corrosion depths in Figure 4.3. The specimens with Material 1 (Figure 4.4a) and Material 2 (Figure 4.4b) with the Type AS gradations in the moist conditions corrode the least and exhibit relatively high resistivity, while Material 3 (Figure 4.4c) has relatively high corrosion depth values but shows relatively low resistivity values. However, the specimen with the Material 4 Type AS gradation in the moist condition (Figure 4.4d) exhibits relatively low corrosion and low resistivity. The specimen with the Material 3 Type BS gradation in the wet condition (Figure 4.4c) exhibits high corrosivity and low resistivity. Resistivity values are considerably lower than Arciniega's resistivity values (reported in Table 3.1) due to the constant addition of DI water to the specimens. The moist specimens were subjected to high humidity throughout the weeks, while the wet specimens required increments of DI water at least once per month.

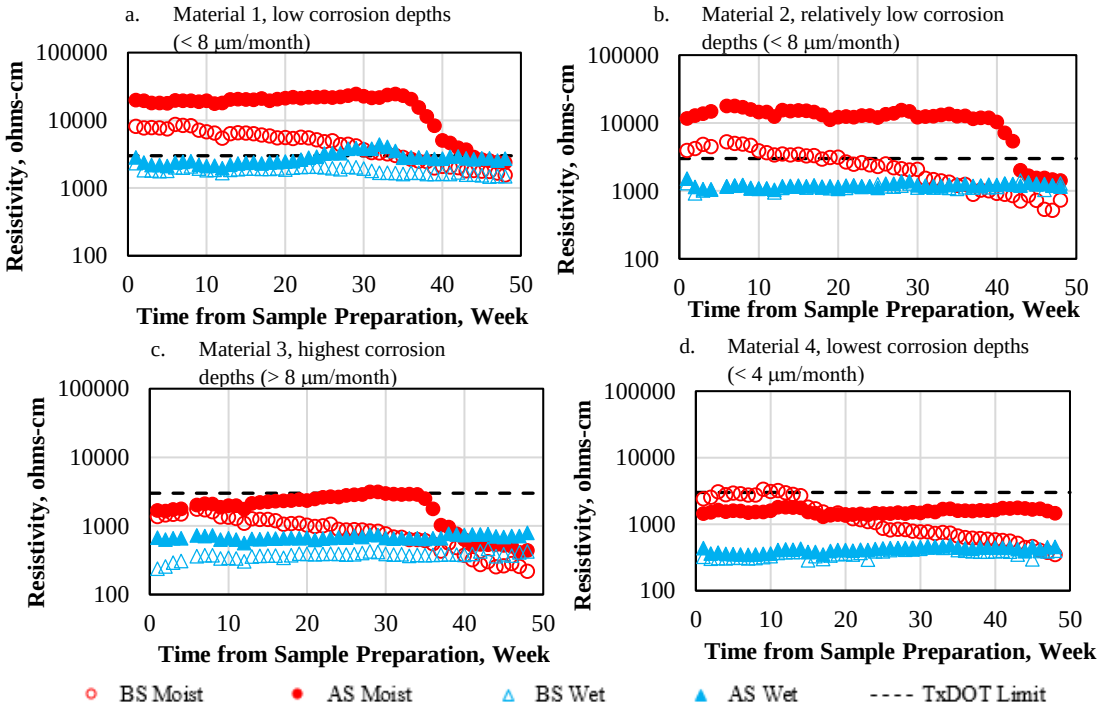


Figure 4.4 Weekly resistivity readings in resistivity instrument

As seen in Figure 4.4, some of the moist specimens (e.g., Material 2 with the AS gradation) exhibit low corrosion depths (less than 2 μm/month) and high resistivity (more than 10000 ohms-cm), as expected. In some wet samples, the relationship is followed. For example, Material 1 wet specimens display both high resistivity (more than 1000 ohms-cm) and low corrosion depth for AS gradation (less than 6 μm/month). However, the majority of the wet specimens do not follow the same relationship. The specimens with Material 4 provide low corrosion depths (less than 4 μm/month) and low resistivity values (less than 1000 ohms-cm) for both gradations under wet condition.

The measured conductivity values of the standing water for the wet specimens are displayed in Figure 4.5. Since low conductivity generally translates to high resistivity, these conductivity values correspond better to the corrosion behavior. The specimens with Material 1 (Figure 4.5a) and Material 2 (Figure 4.5b), which exhibit relatively low corrosion depths in Type BS under wet condition, show low conductivity values. Similarly, the specimens from Material 3 (Figure 4.5c) that have the highest corrosion depths for both gradations under wet condition exhibit high conductivity values. The specimens from Material 4 (Figure 4.5d) exhibit relatively low corrosion depths, low resistivity, and high conductivity values for both gradations under wet condition. Abrupt low conductivity values or fluctuations appear due to the monthly addition of DI water to wet samples.

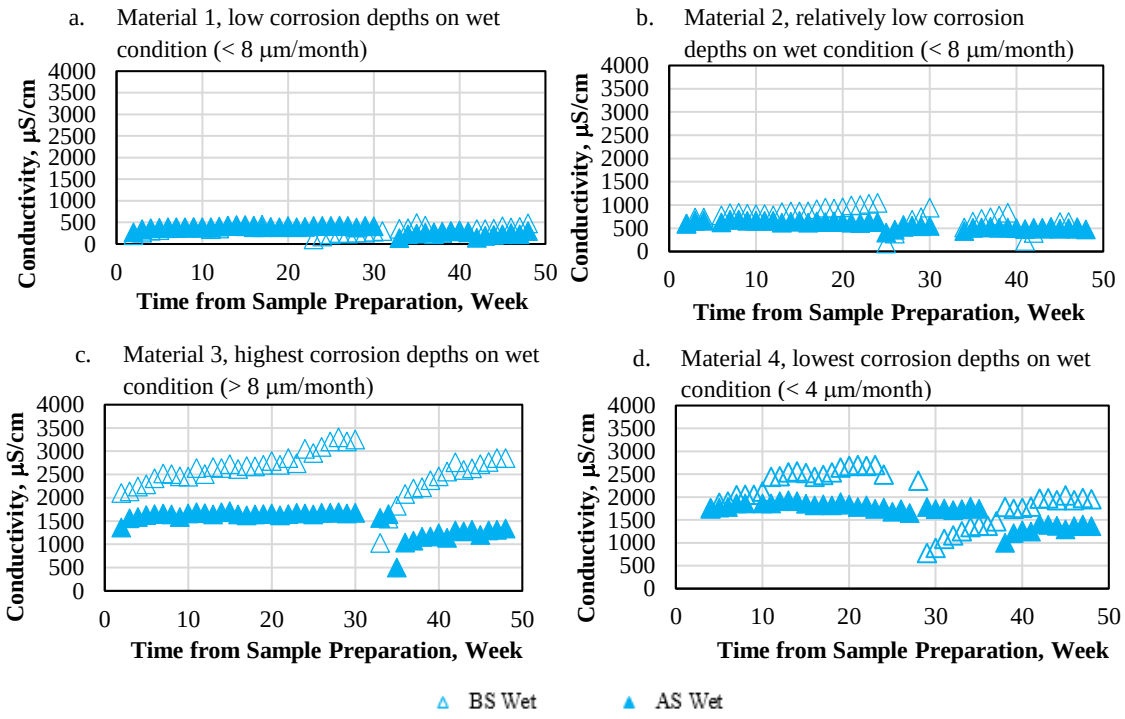


Figure 4.5 Weekly conductivity readings from wet samples

Figure 4.6 shows the correlation between the resistivity measured with the embedded resistivity probes and the corrosion rate as a function of gradation and moisture condition for the four materials. The resistivity of the wet specimens remain relatively constant, while the corrosion rate of these increased significantly. For all materials, the BS gradation wet specimens seem to report lower resistivity values and higher corrosion rates compared to the AS gradation wet specimens. The moist specimens had a different impact according to their gradation and material. In the Material 1 and Material 2 BS gradation moist specimens (Figure 4.6a and Figure 4.6b), resistivity increased significantly, while corrosion rate remained constant for only the initial months. In the Material 3 BS gradation moist specimens (Figure 4.6c), resistivity increased significantly and high corrosion rates were reported. In the Material 4 BS gradation moist specimens (Figure 4.6d), both resistivity and corrosion rate decreased significantly. In the AS gradation moist specimens of all materials, resistivity increased as corrosion rate decreased.

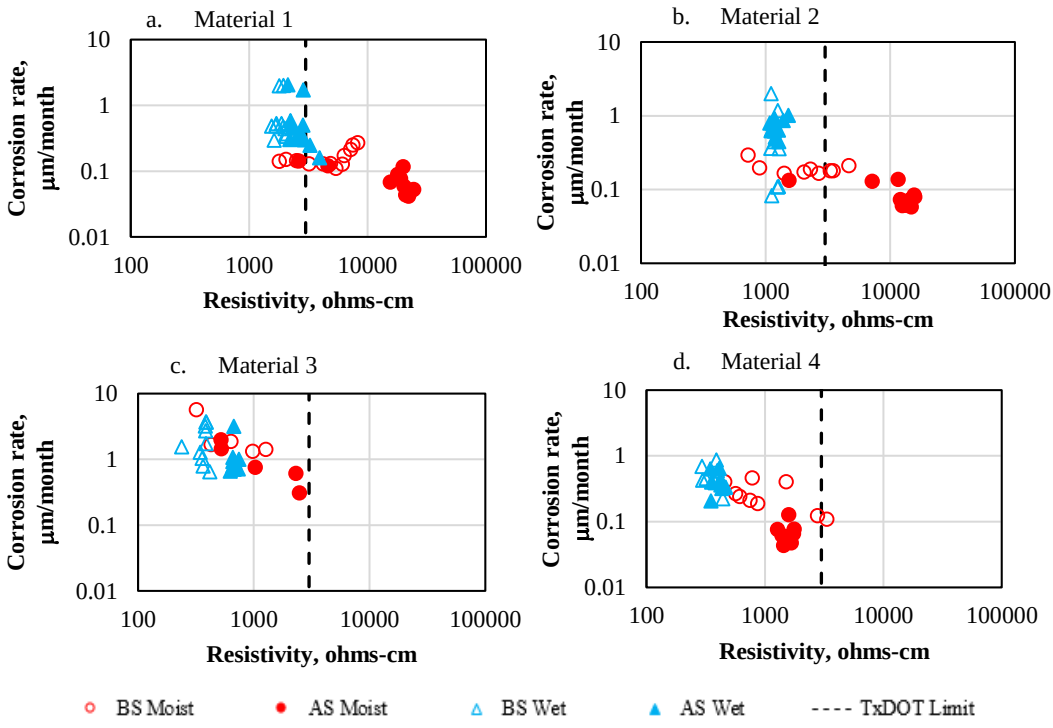


Figure 4.6 Resistivity and corrosion rate correlations

Figure 4.7 shows the correlation between the conductivity readings from the standing water of the wet samples and the corrosion rate as a function of gradation for the four materials. Scatter is present on Figure 4.7 due to the frequent DI water additions to the wet specimens. Variations are mainly observed on the BS gradation of Material 1 (4.7a) and Material 2(4.7b), where conductivity values are increasing and decreasing without a trend. However, the AS gradation of Material 1 and 2 have low conductivity values along with low corrosion rates. Material 3 (Figure 4.7c) showed increasing conductivity and corrosion rate for the most part on the BS gradation, however, showed relatively constant corrosion rate and increasing conductivity on the AS gradation. Material 4 (Figure 4.7d) reported high conductivity and low corrosion rates on both gradations.

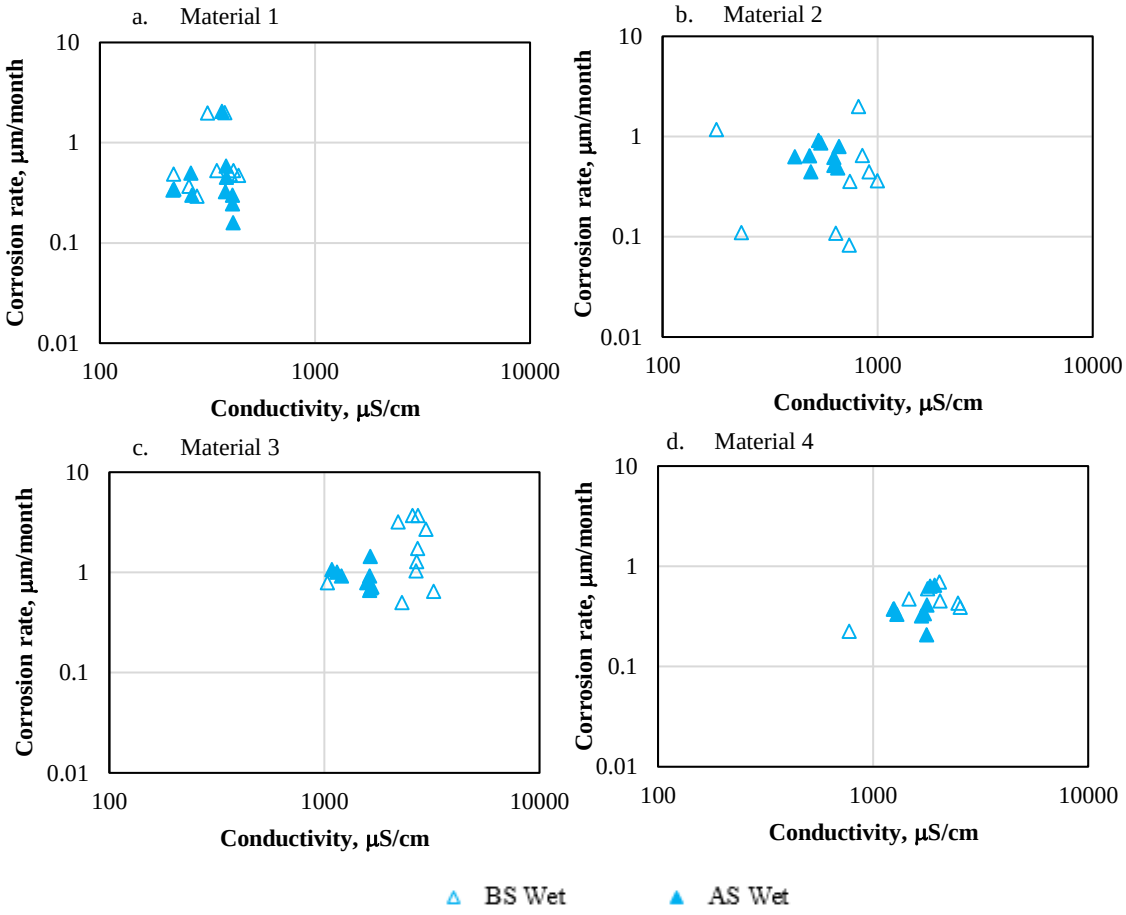


Figure 4.7 Conductivity and corrosion rate correlations

## 4.2 ANALYSES OF MODELS

The relationships between the Tafel and LPR current density estimation models discussed in Section 3.3 are compared in this section. The models' current densities and corrosion rates were estimated at the following overpotential windows: ±30 mV, ±50 mV, ±70 mV, ±90 mV, ±110 mV, and ±130 mV. As an example, Figure 4.8 shows the correlation between the corrosion rates estimated using Model 1 at a ±130 mV overpotential window and those estimated at a ±30 mV overpotential window. The two corrosion rates are well correlated with a coefficient of determination ($R^2$) of 0.97. At the same time, the corrosion rate estimated with the ±30 mV overpotential is 22% (slope of best fit line of 0.22) of the corrosion rate with overpotential of ±130 mV. An increase in slope appears with an increase in overpotential window. Therefore, corrosion rates estimated at a larger overpotential window will report higher corrosion rates.

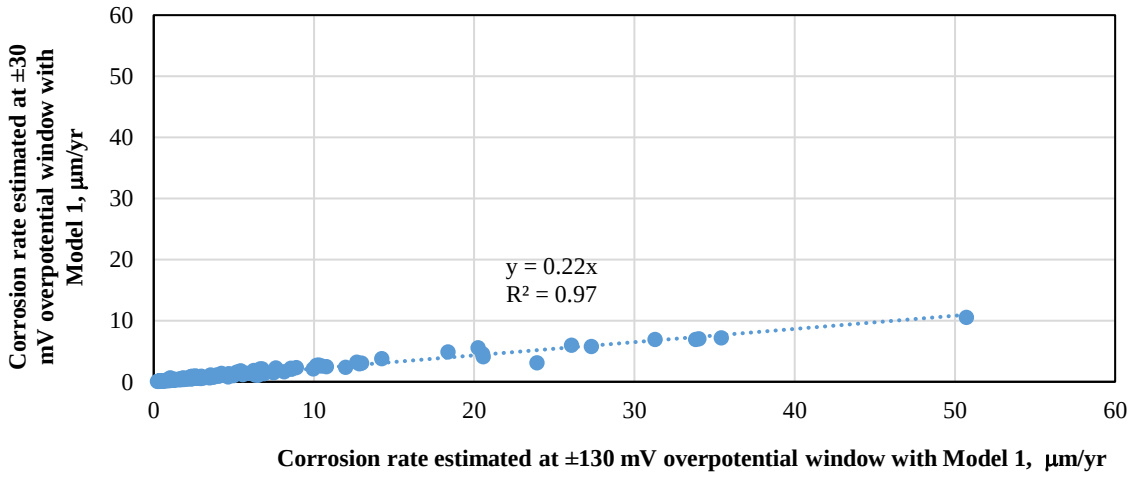


Figure 4.8 Correlation of corrosion rates estimated at ±130 mV overpotential window and ±30 mV overpotential window using Model 1

Table 4.1 shows the correlations between the estimated corrosion rates at a ±130 mV overpotential window and the estimated corrosion rates for other overpotential windows for Model 1. The normalized rate of corrosion, or slope of the regression, increases with increasing

overpotential window. Thus, the rate of corrosion decreases as the overpotential window decreases. For all overpotential window comparisons, the two corrosion rates are well correlated with high coefficients of determination (i.e. $R^2$ higher than 0.97). The low standard error of estimate (SEE) values indicate low variability between overpotential windows.

Table 4.1 Correlations of Model 1 corrosion rates estimated at different overpotential windows

| Overpotential, mV | Normalized Rate of Corrosion* | $R^2$ | Standard Error of Estimate (SEE) |
|---|---|---|---|
| ±30 | 0.22 | 0.97 | 0.27 |
| ±50 | 0.39 | 0.97 | 0.47 |
| ±70 | 0.56 | 0.98 | 0.61 |
| ±90 | 0.74 | 0.95 | 1.30 |
| ±110 | 0.87 | 0.99 | 0.77 |

*Corrosion rate at a given overpotential/corrosion rate at ±130 mV overpotential

To validate that corrosion rate linearly decreases with overpotential decrease, Tafel slopes were observed. Table 4.2 shows the estimated Tafel slopes values for each overpotential window for Material 4. Table 4.2 indicates that the Tafel slopes decrease with decreasing overpotential window, which causes the intersection of the Tafel slopes to move toward decreasing current densities, therefore lower corrosion rates.

Table 4.2 Material 4 estimated Tafel slopes

| Tafel slope, V/decade | Specimen | Overpotential, mV | | | | | |
|---|---|---|---|---|---|---|---|
| | | ±30 | ±50 | ±70 | ±90 | ±110 | ±130 |
| Anodic | BS Moist | 0.051 | 0.088 | 0.114 | 0.124 | 0.146 | 0.150 |
| | AS Moist | 0.051 | 0.097 | 0.136 | 0.183 | 0.213 | 0.238 |
| | BS Wet | 0.057 | 0.118 | 0.183 | 0.232 | 0.288 | 0.289 |
| | AS Wet | 0.052 | 0.093 | 0.135 | 0.165 | 0.176 | 0.167 |
| Cathodic | BS Moist | 0.063 | 0.110 | 0.157 | 0.196 | 0.230 | 0.262 |
| | AS Moist | 0.059 | 0.105 | 0.147 | 0.184 | 0.217 | 0.250 |
| | BS Wet | 0.054 | 0.088 | 0.117 | 0.140 | 0.152 | 0.164 |
| | AS Wet | 0.060 | 0.101 | 0.138 | 0.170 | 0.195 | 0.215 |

Similar to Table 4.1, Appendix A contains the correlations with different overpotential windows of all models. The slopes of the ±130 mV overpotential window vs. each overpotential window decrease for Models 1, 2, 3, and 5; therefore, corrosion rates linearly decrease as the overpotential window decreases. Overall, all models are well correlated (i.e. $R^2$ values greater than 0.94). The low SEE values indicate a low level of variability for the estimated corrosion rates of each overpotential window in comparison to the ±130 mV overpotential window.

Figure 4.9 shows the correlation between the corrosion rates estimated using Model 1 and Model 2 at a ±130 mV overpotential window. The corrosion rates estimated from the two models are well correlated with a bias of 13%. Similar results but from other overpotentials are summarized in Table 4.3. All models are well correlated as judged by coefficients of determination ($R^2$ values) of 0.98 and greater. The slopes between the two measurements, corresponding to the bias among the results from the two models are within the narrow ranges of 1.13 to 1.18.

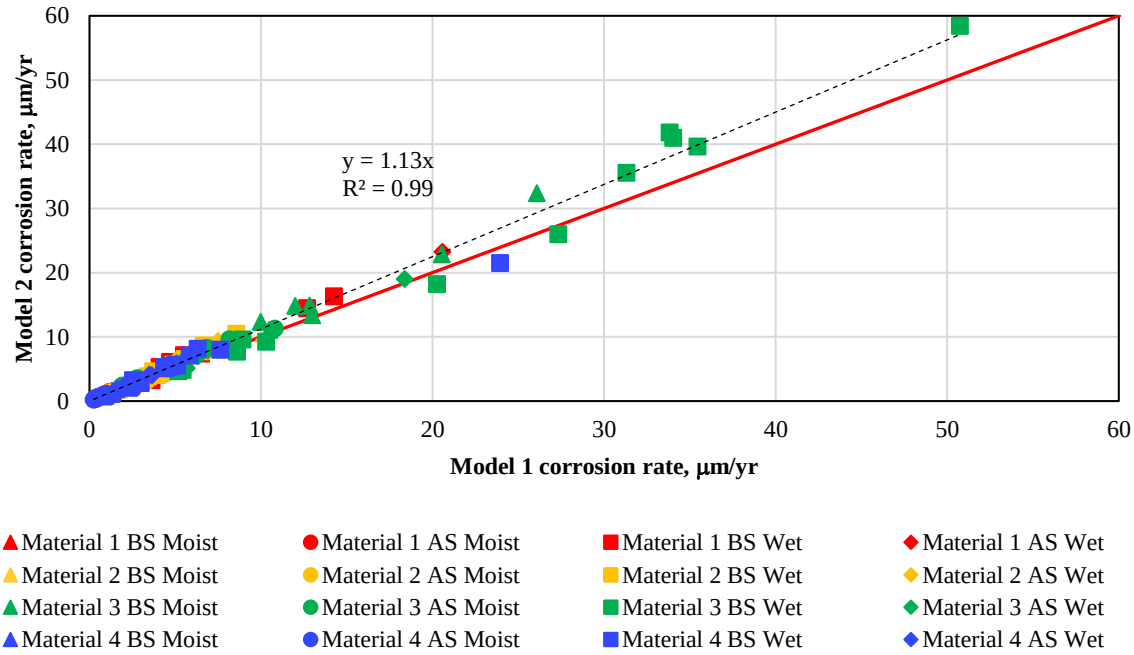


Figure 4.9 Correlation between Model 1 and Model 2 corrosion rates at a 130 mV overpotential window

Table 4.3 Relationship parameters between Model 1 and Model 2 corrosion rate estimations with increasing overpotential window

| Overpotential window, mV | Slope | $R^2$ | Standard Error of Estimate (SEE) |
|---|---|---|---|
| ±30 | 1.18 | 1.00 | 0.11 |
| ±50 | 1.16 | 1.00 | 0.27 |
| ±70 | 1.17 | 1.00 | 0.38 |
| ±90 | 1.14 | 0.98 | 0.76 |
| ±110 | 1.15 | 0.99 | 0.70 |
| ±130 | 1.13 | 0.99 | 0.75 |

Figure 4.10 shows the correlation between corrosion rates estimated using Model 1 and corrosion rates from Model 5 at a ±130 mV overpotential window. Table 4.4 reports high correlation on all overpotential windows. The slope decreases with increasing overpotential window, indicating that Model 5 estimates higher current density values at regions closer to an LPR region (±30 mV and ±50 mV). As seen previously, the SEE decreases as the overpotential window decreases. Model 5 predicts higher corrosion rate values at lower overpotential windows, but reports the highest correlation for these cases.

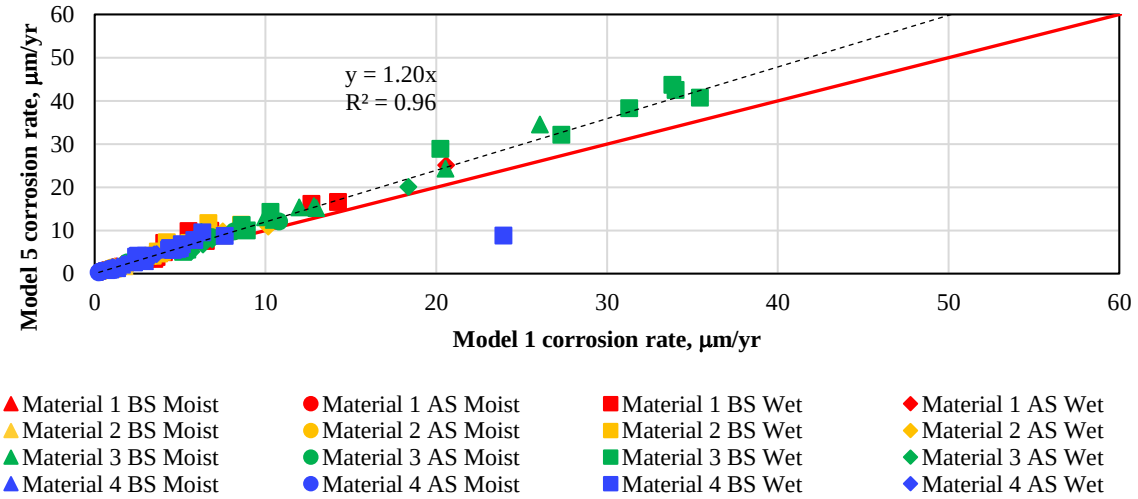


Figure 4.10 Correlation between Model 1 and Model 5 corrosion rates at a 130 mV overpotential window

Table 4.4 Relationship parameters between Model 1 and Model 5 corrosion rate estimations with increasing overpotential window

| Overpotential Window, mV | Slope | $R^2$ | Standard Error of Estimate (SEE) |
|---|---|---|---|
| ±30 | 1.35 | 1.00 | 0.14 |
| ±50 | 1.28 | 0.99 | 0.34 |
| ±70 | 1.27 | 0.99 | 0.50 |
| ±90 | 1.21 | 0.98 | 1.00 |
| ±110 | 1.25 | 0.99 | 0.64 |
| ±130 | 1.20 | 0.96 | 1.39 |

Figure 4.11 shows the correlation between corrosion rates estimated using Model 3 and corrosion rates from Model 4 at a ±130 mV overpotential window. Noted in Section 3.3, Model 4 current densities were always estimated at ±10 mV overpotential window. This means that the corrosion rates from Model 4 are kept constant for all overpotential windows, however the corrosion rates of Model 4 differ between material, condition, and gradation. Table 4.5 shows high correlation on all overpotential windows, mainly on the ±30 and ±50 mV overpotential windows. The slope decreases and the SEE increases with increasing overpotential window. At a ±70 mV overpotential window, Model 4 gives values that are half of the Model 3 values. The low slope values of Model 4 indicate a representative approximation to the traditional LPR model (Model 3) without the need to use Tafel slopes.

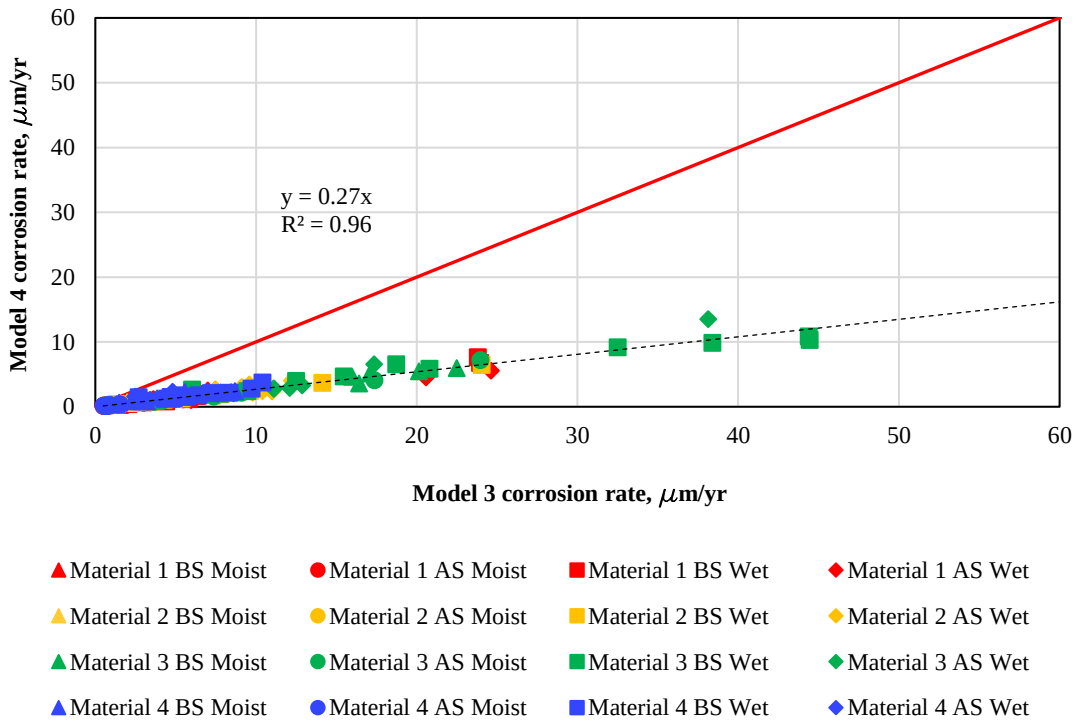


Figure 4.11 Correlation between Model 3 and Model 4 corrosion rates at a 130 mV overpotential window

Table 4.5 Relationship parameters between Model 3 and Model 4 corrosion rate estimations with increasing overpotential window

| Overpotential window, mV | Slope | R2 | Standard Error of Estimate (SEE) |
|---|---|---|---|
| ±30 | 1.11 | 1.00 | 0.23 |
| ±50 | 0.61 | 0.99 | 0.32 |
| ±70 | 0.49 | 0.98 | 0.63 |
| ±90 | 0.35 | 0.96 | 0.56 |
| ±110 | 0.30 | 0.95 | 0.61 |
| ±130 | 0.27 | 0.96 | 0.49 |

## 4.3 MEASURED THICKNESSES

### 4.3.1 Magnetic Probe Measurements

Zinc thickness readings were initially recorded on sacrificial coupons after the specimen's construction using the *Elcometer 456 Coating Thickness Gauge*$^{TM}$. Figure 4.12 shows box plots representing the 16 initial zinc thickness probe readings for each coupon. Overall, the initial zinc thickness readings are in the wide range of 58 μm to 135 μm (2 mils to 5 mils).

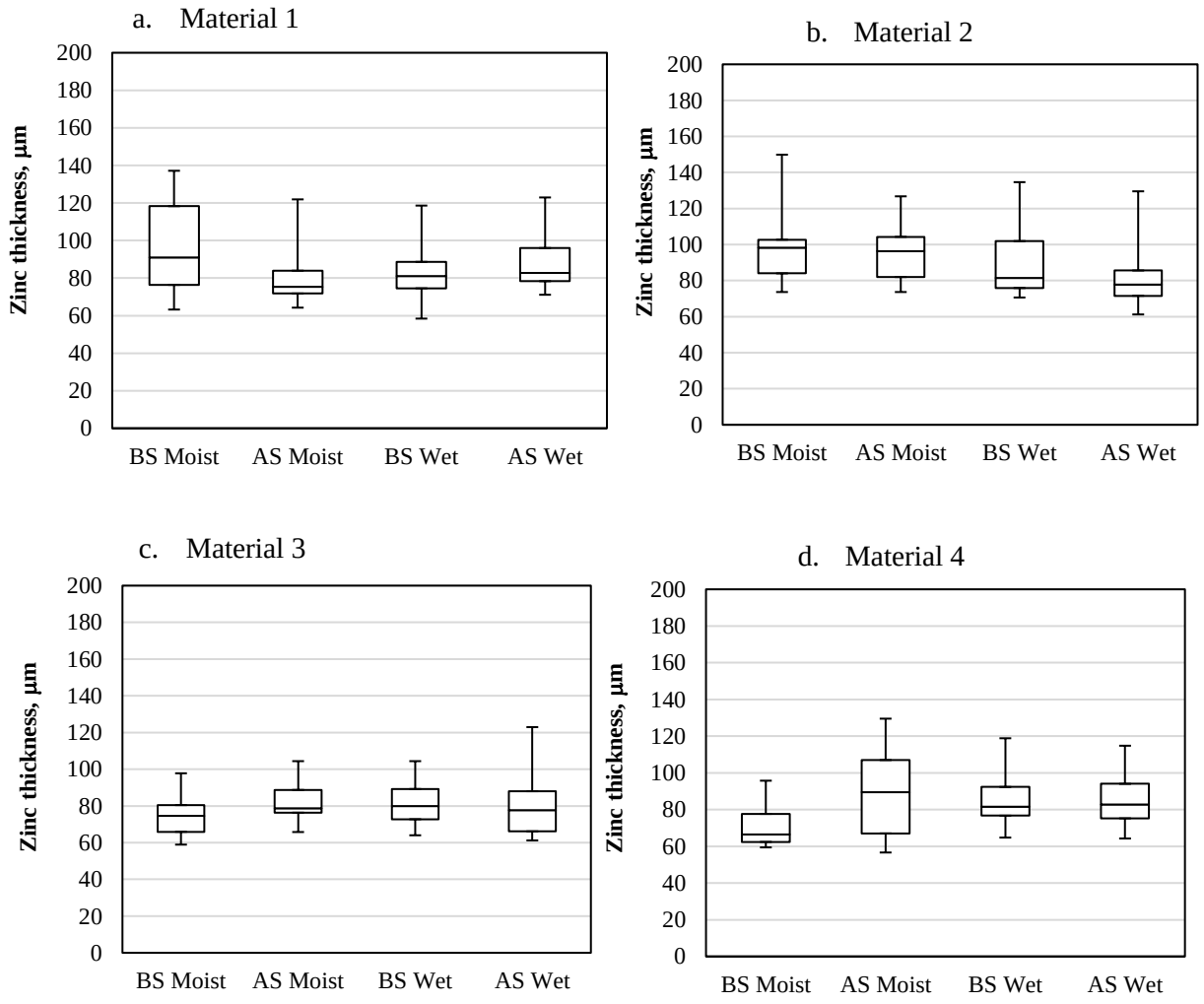


Figure 4.12 Probe initial zinc thickness readings

### 4.3.2 Scanning Electron Microscope (SEM) Images

SEM images were obtained from the sacrificial coupons exhumed from each cylindrical specimen after a period of 6 months. Figure 4.13 shows close-up SEM images from the four Material 2 sacrificial coupons. The BS gradation of all materials, except Material 3, reported narrower SEM zinc thickness measurements on the wet condition (Figure 4.13b) compared to the moist condition (Figure 4.13a), indicating higher zinc thickness losses on the wet condition. Similarly, the AS gradation of all materials, except Material 3, showed narrower zinc thickness measurements on the wet condition (Figure 4.13d) compared to the moist condition (Figure 4.13c). Some coupons are affected by cracking (Figure 4.13d), which lead to weaker zinc layers. The SEM images for the complete observed length of each of the sixteen sacrificial coupons are shown in Appendix B.

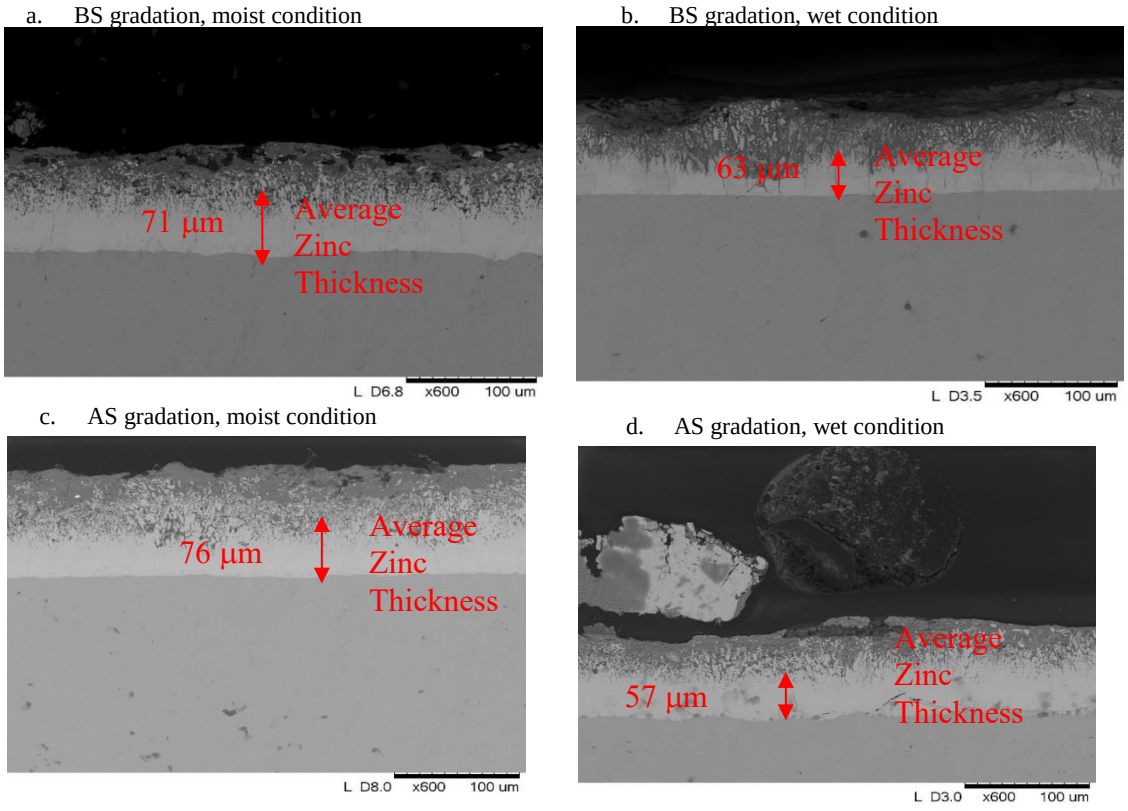


Figure 4.13 SEM close-up images from Material 2 sacrificial coupons

# Chapter 5: Conclusions

## 5.1 SUMMARY

The service life of MSE walls is affected by many factors such as the corrosion of galvanized reinforcements. The goal of this work consisted on evaluating and assessing rate of corrosion, and possibly proposing a protocol to estimate the rate of corrosion of MSE wall reinforcements accurately and systematically. This study was also focused on studying the corrosion rate, resistivity, and conductivity to evaluate the corrosion behavior of galvanized steel embedded in different moisture conditions and gradations.

To achieve the goal, a systematic data collection of Tafel and LPR tests was produced for one year. From these electrochemical tests, five models were developed to estimate the corrosion rate of galvanized reinforcements. It was also desired to possibly obtain relationships between the estimated corrosion rate, resistivity, and conductivity. In addition, a systematic data collection of zinc thickness measurements of galvanized reinforcements was acquired to ultimately propose practices to analyze these collected data in order to estimate zinc thickness loss (i.e. cumulative corrosion) of the reinforcements. Ultimately, it was desired to possibly select a model that best correlated between the estimated cumulative corrosion and the measured cumulative corrosion of galvanized reinforcements.

## 5.2 CONCLUSIONS

Upon the completion of testing and analyzing results of the laboratory procedure, the following observations and conclusions are presented:

- Cumulative corrosion of galvanized reinforcements is higher when BS gradation is selected in comparison to AS gradation for both moist and wet conditions on all four materials.
- Cumulative corrosion of wet specimens is higher than cumulative corrosion of moist specimens.
- Material 1 and 2, which had high resistivity in Arciniega's study, reported low corrosion depths in this study; at the same time, Material 3, which was a low resistivity material in Arciniega's study, resulted in the highest corrosion depths in this study.
- Material 1 and Material 2 specimens with the Type AS gradations in the moist conditions are the least corrosive and exhibit relatively high resistivity, while Material 3 has relatively high corrosion depth values but shows relatively low resistivity values.
- The specimen with the Material 3 Type BS gradation in the wet condition exhibited high corrosivity and low resistivity.
- For the most part, conductivity readings followed the expected behavior of high/low conductivity readings leading to high/low corrosion rates. This behavior appeared on Material 1 and Material 2 specimens, which exhibited low corrosion rates and low conductivity readings in Type BS under wet condition. Similarly, Material 3 specimens, which have the highest corrosion rates for both gradations under wet condition, exhibited high conductivity values.

- Material 4, which is the lowest resistivity material according to Arciniega's study, resulted with the lowest corrosion depths, low resistivity values, and the highest conductivity readings. Material 4 did not achieve the expected behavior.

Upon the completion of the five models analyses, the following observations and conclusions are presented:

- For all models, a decrease in slope appeared with a decrease in overpotential window. Therefore, corrosion rates estimated at a lower overpotential window will report lower corrosion rates.
- The corrosion rates estimated with Model 1 and Model 2 are well correlated with a bias of 13%. These two models observed at different overpotential are well correlated as judged by coefficients of determination ($R^2$ values) of 0.98 and greater.
- When comparing Model 1 to Model 5, the slope decreases with increasing overpotential window, indicating that Model 5 estimates higher current density values at regions closer to an LPR region (±30 mV and ±50 mV).
- Model 4 low slope values indicate a representative approximation to the traditional LPR model (Model 3) without the need to use Tafel slopes.

Upon the completion of the measured thicknesses collection, a practice to analyze the collected zinc thickness data (i.e. probe readings and SEM readings) to obtain actual cumulative corrosion was not achieved. A high variability of the initial zinc thickness readings obtained with the probe was observed for all samples. The difference between the initial zinc thickness reading (probe) and the final zinc thickness reading (SEM) was the actual cumulative corrosion. This

meant that actual cumulative values relied on the variability of the initial zinc thickness readings, therefore a comparison could not be performed.

## 5.3 RECOMMENDATIONS

The following recommendations are suggested to further assess the corrosion behavior of galvanized steel reinforcements:

- Perform corrosion analyses for the galvanized mesh and epoxy-coated rebar working electrodes of all materials.
- Conduct ion chromatography tests and other chemical tests on the leachates of the wet specimens to obtain information on the chloride and sulfate content and the presence of carbonates in the materials.
- Perform additional analyses on Material 4 to provide explanation on its behavior (lowest corrosion depths, low resistivity, and highest conductivity).
- Resistivity values from this study are considerably lower than Arciniega's resistivity values due to the constant addition of DI water to the specimens. This also affected the conductivity readings. To solve this issue, the soil humidity can be recorded weekly in order to make any corrections on the readings.

The following recommendations are suggested to further select the best practice to estimate the rate of corrosion of galvanized steel reinforcements:

- If SEM imaging is desired to measure the actual cumulative corrosion, obtain a set of SEM images as initial readings (when specimen is brand new), a set of SEM images 6 months after, and another set of SEM images 12 months after.
- If other methods are desired to measure the actual cumulative corrosion, weight loss measurements can be used.

# References


Alzamora, D.E. and Anderson S.A. (2009) “Review of Mechanically Stabilized Earth Wall Performance Issues” Transportation Research Board, Washington, D. C.

American Galvanizers Association (AGA) (2018) “Types of Corrosion” Retrieved from Web. https://galvanizeit.org/corrosion/corrosion-process/types-of-corrosion

Anderson, P. L., Gladstone, R. A., and Sankey, J.E. (2012) “State of the Practice of MSE Wall Design for Highway Strcutures” GeoCongress 2012, Oakland, CA

Arciniega, J. L. (2017) “Invited Student Paper - Impact of Grain Size Distribution on Resistivity of Mechanically Stabilized Earth Wall Backfill Materials” Transportation Research Board, Washington, D.C.

Arciniega, J. L., Walker, W. S., Nazarina, S., and Fishman, K. L. (2018) “A Process for Optimizing Gradation of Marginal Backfill of Mechanically Stabilized Earth Walls to Achieve Acceptable Resistivity” Transportation Research Record: Journal of the Transportation Research Board

Baboian, R. (1995) “Corrosion Tests and Standards: Application and Interpretation” ISBN 0-8031-2058-3, U.S.A.

Bard, A. J., and Faulkner, L. R. (1980) “Electrochemical Methods: Fundamentals and Applications” First Edition, ISBN 0-471-05542-5, U. S. A.

Bard, A. J., and Faulkner, L. R. (2001) “Electrochemical Methods: Fundamentals and Applications” Second Edition, ISBN 0-471-04372-9, U.S.A.

Beckham, T. L., Sun, L., and Hopkins, T. C. (2005) “Corrosion Evaluation of Mechanically Stabilized Earth Walls” KTC-05-28/SPPR 239-02-1F, University of Kentucky, U.S.A.

Berg, R. R., Christopher, B. R., Samtani, N. C. (2009) “Design of Mechanically Stabilized Earth Walls and Reinforced Soil Slope – Vol II” National Highway Institute, Federal Highway Administration, Washington, D.C.

Berke, B. S. and Sagüés, A. A. (2009) “Update on Condition of Reinforced Earthwall Straps” Florida Department of Transportation, University of South Florida, Tampa, FL

Borrok, D., Bronson, A., and Nazarian, S. (2013) “Characterization of Coarse Backfill Materials for Prevention of Corrosion of MSE Metallic Wall Reinforcement” Project No. 0-6359. Center for Transportation Infrastructure Systems, The University of Texas at El Paso, El Paso, TX.

Briaud, J. L., Sanchez, M., Aghahadi, M., Bi, G., and Huang, J. (2017) “Interaction Between Drilled Shaft and Mechanically Stabilized Earth (MSE) Wall: Technical Report” FHWA/TX-15/0-6715-1. Texas A&M Transportation Institute, College Station, TX.

Budinksi, K. G. and Budinski, M. K. (2002) “Engineering Materials: Properties and Selection” Seventh Edition ISBN 0-13-030533-2, U.S.A.

Butler, J.A. V. (1924) “Studies in Heterogeneous Equilibria. Part II. The Kinetic Interpretation of the Nernst Theory of Electromotive Force” Trans. Faraday Society, 19, 729-733

Corrosionpedia (2018) “Dry Film Thickness (DFT)” Retrieved from Web. <https://www.corrosionpedia.com/definition/1249/dry-film-thickness-dft>

Elias, V., Fishman, K. L., Christopher, B. R., and Berg, R. R. (2009) “Corrosion/Degradation of Soil Reinforcements for Mechanically Stabilized Earth Walls and Reinforced Soil Slopes” FHWA-SA-96-072, Federal Highway Administration, Washington, D.C.

Erdey-Gruz, T., and Volmer, M. (1930) “Zur theorie der wasserstoffüberspannung.” Z. Phys. Chem., 150 (A), 203-213

Fischer Technology Inc. (2018) “Magnetic Induction Process” Retrieved from Web. <http://www.fischer-technology.com/en/united-states/knowledge/methods/coating-thickness-measurement/magnetic-induction-process/>

Fishman, K. L. and Withiam, J. L. (2011) “LRFD Metal Loss and Service-Life Strength Reduction Factors for Metal-Reinforced Systems” NCHRP Report 675, Transportation Research Board, Washington, D.C.

Galvan, M. (2011) “MSE retaining wall design considerations” Presentation. Texas Department of Transportation, TX.

Gladstone, R. A., Anderson, P. L., Fishman, K. L., and Withiam, J. L. (2006) “Durability of Galvanized Soil Reinforcement: More Than 30 Years of Experience with Mechanically Stabilized Earth” Transportation Research Record 1975, Washington, D.C.

Johnston, D. (2005) “Corrosion Monitoring of Hot Springs VSL Mechanically Stabilized Earth Wall” SD2004-02-F, South Dakota Department of Transportation, U.S.A.

Jones, D. A. (1992) “Principles and Prevention of Corrosion” ISBN 0-02-361215-0, U.S.A.

King, R. A. (1977) “A Review of Soil Corrosiveness with Particular Reference to Reinforced Earth” TRRL Supplementary Report 316, Transport and Road Research Laboratory, Crowthorne, Berkshire, England

Mansfeld, F., and Oldham, K. B. (1971) “A Modification of the Stern-Geary Linear Polarization Equation” Corrosion Science, Vol. 11, pp. 787-797 Great Britain

Marcus, P. (2012) “Corrosion Mechanisms in Theory and Practice” Third Edition. ISBN 978-1-4200-9463-3

Pistofidis, N., Vourlias, G., Konidaris, S., Pavlidou, E., Stergiou, A., and Stergioudis, G. (2005) “Microstructure of Zinc Hot-Dip Galvanized Coatings Used for Corrosion Protection” Materials Letters 60 (2006) 786-789

Raeburn, C. L., Monkul, M. M., Pyles, M.R. (2008) “Evaluation of Corrosion of Metallic Reinforcements and Connections in MSE Retaining Walls” Project 643, Oregon Department of Transportation, Salem, OR

Sokolic, I. Poor, N., Gunaratne M., and Rajaguru, T. (2015) “Distribution of Chloride, pH, Resistivity, and Sulfate Levels in Backfill for Mechanically-Stabilized Earth Walls and Implications for Corrosion Testing” Department of Civil & Environmental Engineering University of South Florida, U.S.A.

Soriano, C. and Alfantazi, A. (2015) “Corrosion Behavior of Galvanized Steel Due to Typical Soil Organics” Department of Materials Engineering, University of British Columbia, Vancouver, B.C.

Stansbury, E. E. and Buchanan, R. A. (2000) “Fundamentals of Electrochemical Corrosion” ISBN 0-87170-676-8

Stern, M., and Geary, A. L. (1975) “Electrochemical Polarization I. A Theoretical Analysis of the Shape of Polarization Curves” Journal of Electrochemical Society, Vo. 104, No. 1, pp.56-62, U.S.A.

Sun, C. and Graves C. (2013) “Evaluation of Mechanically Stabilized Earth (MSE) Walls for Bridge Ends in Kentucky; What Next?” Research Report KTC-13-11/SPR443-12-1F. Kentucky Transportation Center, Lexington, KY.

Thornley, J.D. and Siddharthan, R.V. (2010) “Effects of Corrosion Aggressiveness on MSE Wall Stability in Nevada” Earth Retention Conference 2010, Bellevue, Washington, U.S.A.

Todokoro, H. and Ezumi, M. (1996) “Scanning Electron Microscope” US5900629A

# Appendix A: Analyses of Models Results

Table A1 Correlations of models corrosion rates estimated at different overpotential windows

| Model | Overpotential, mV | Normalized Rate of Corrosion (Corrosion rate at a given overpotential/corrosion rate at ±130 mV overpotential) | $R^2$ | Standard Error of Estimate (SEE) |
|---|---|---|---|---|
| 1 | ±30 | 0.22 | 0.97 | 0.27 |
| | ±50 | 0.39 | 0.97 | 0.47 |
| | ±70 | 0.56 | 0.98 | 0.61 |
| | ±90 | 0.74 | 0.95 | 1.30 |
| | ±110 | 0.87 | 0.99 | 0.77 |
| 2 | ±30 | 0.22 | 0.95 | 0.42 |
| | ±50 | 0.41 | 0.96 | 0.71 |
| | ±70 | 0.60 | 0.97 | 0.84 |
| | ±90 | 0.77 | 0.96 | 1.33 |
| | ±110 | 0.89 | 0.99 | 0.92 |
| 3 | ±30 | 0.25 | 0.96 | 0.49 |
| | ±50 | 0.45 | 0.97 | 0.78 |
| | ±70 | 0.63 | 0.97 | 0.95 |
| | ±90 | 0.78 | 0.98 | 1.07 |
| | ±110 | 0.92 | 0.99 | 0.89 |
| 5 | ±30 | 0.24 | 0.97 | 0.37 |
| | ±50 | 0.44 | 0.98 | 0.62 |
| | ±70 | 0.62 | 0.97 | 0.92 |
| | ±90 | 0.76 | 0.94 | 1.78 |
| | ±110 | 0.89 | 0.96 | 1.69 |

# Appendix B: SEM Results

a. BS moist sample

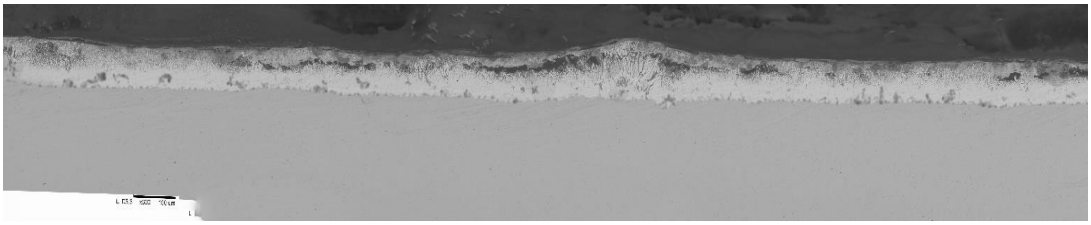

b. AS moist sample

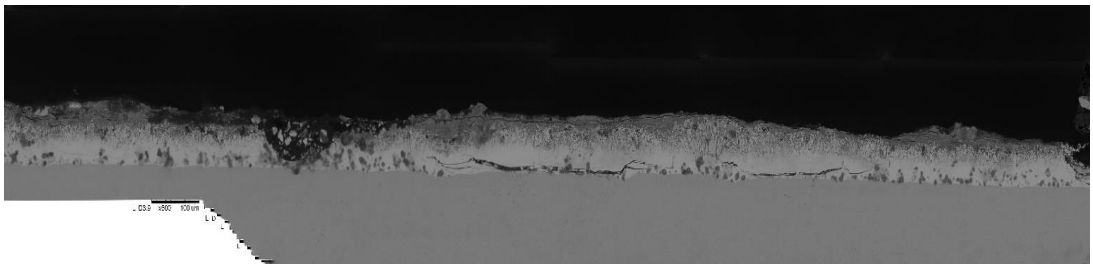

c. BS wet sample

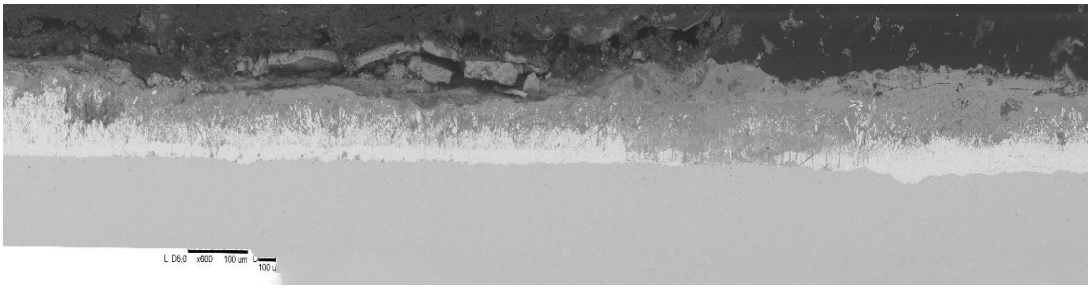

d. AS wet sample

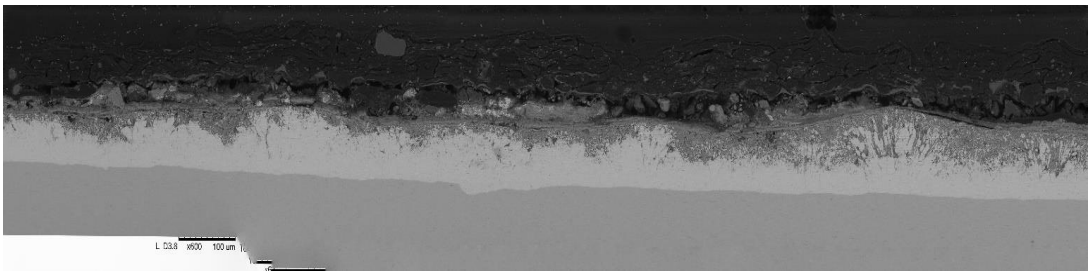

Figure B1 Material 1 sacrificial coupons exhumed after 6 months

a. BS moist sample

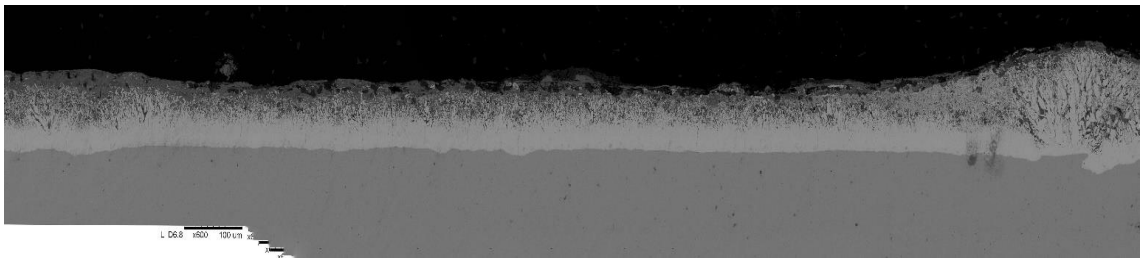

b. AS moist sample

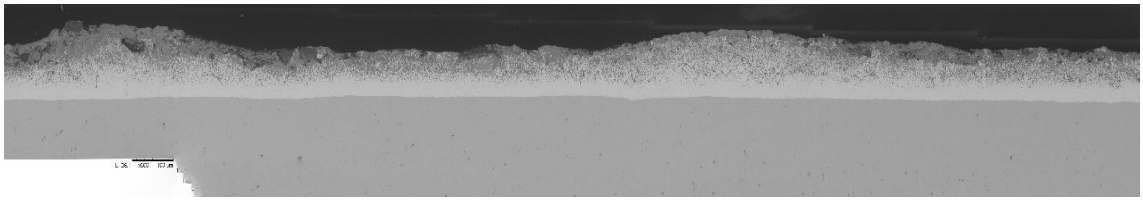

c. BS wet sample

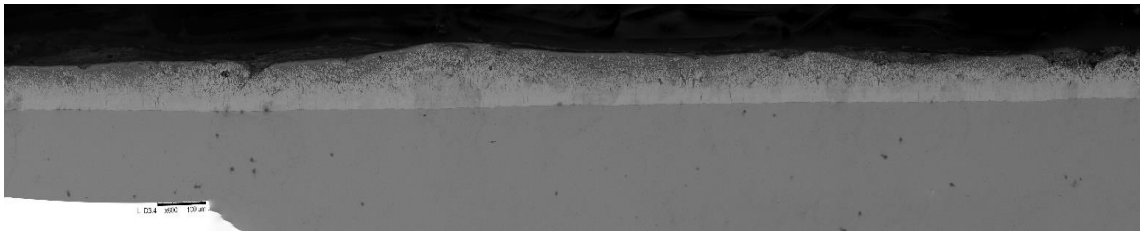

d. AS wet sample

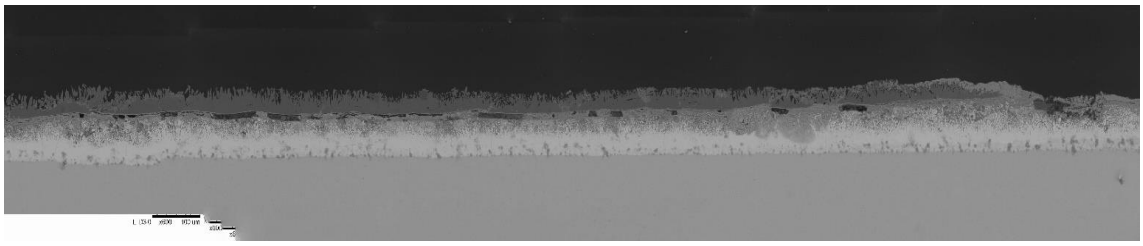

Figure B2 Material 2 sacrificial coupons exhumed after 6 months

a. BS moist sample

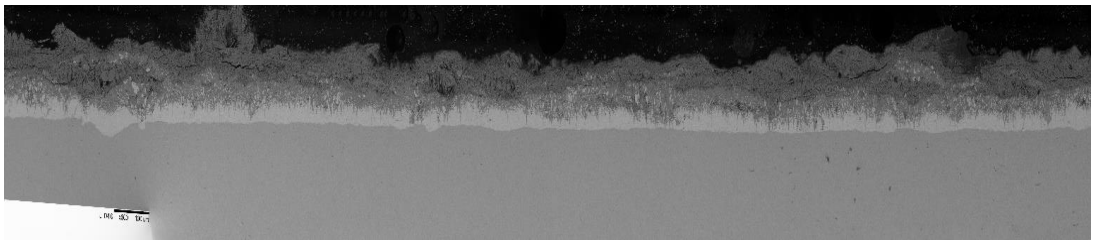

b. AS moist sample

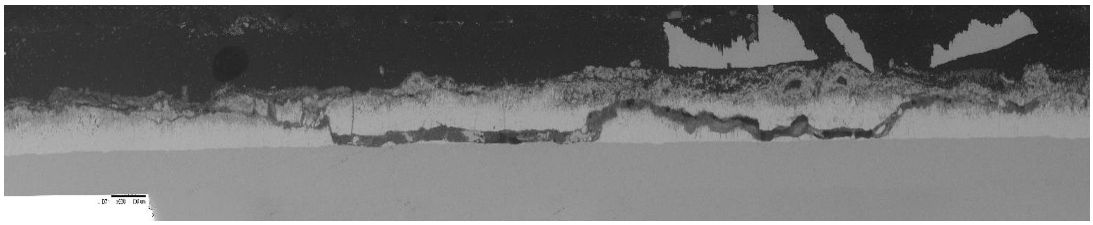

c. BS wet sample

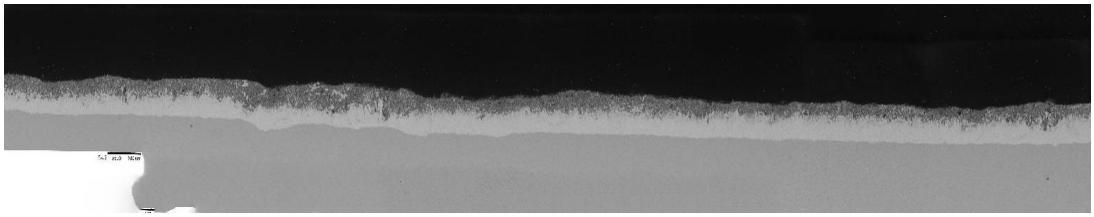

d. AS wet sample

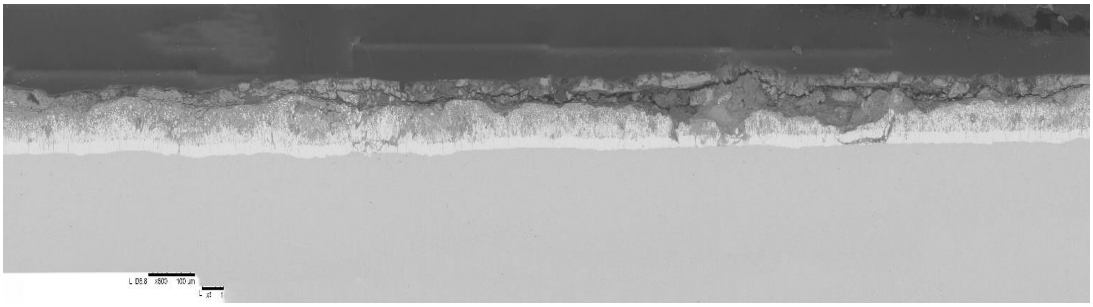

Figure B3 Material 3 sacrificial coupons exhumed after 6 months

a. BS moist

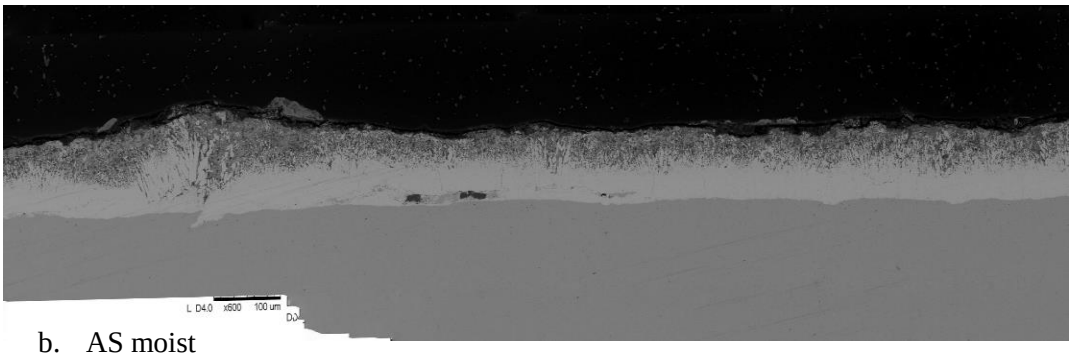


b. AS moist

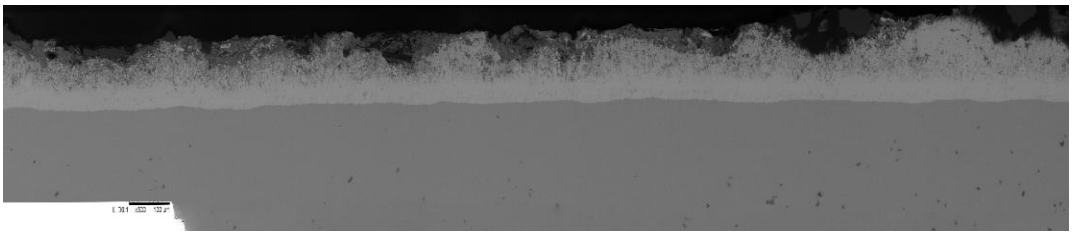

c. BS wet

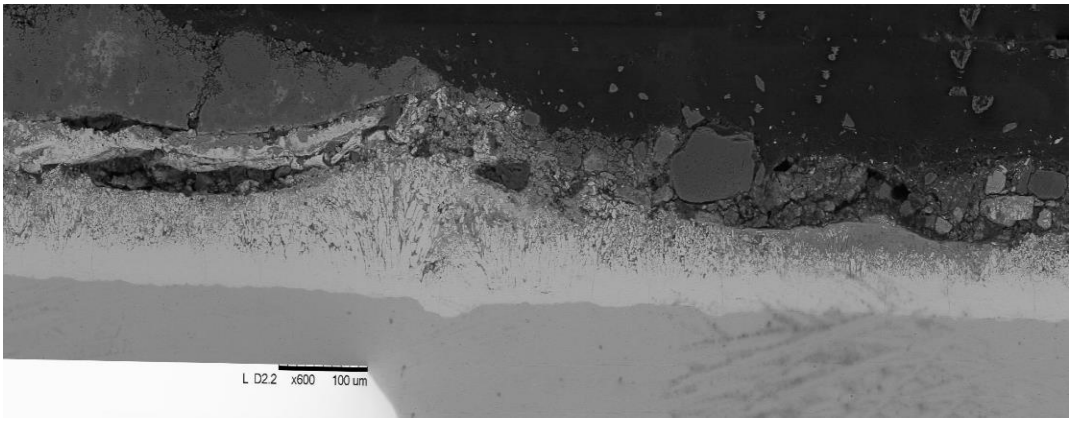


d. AS wet

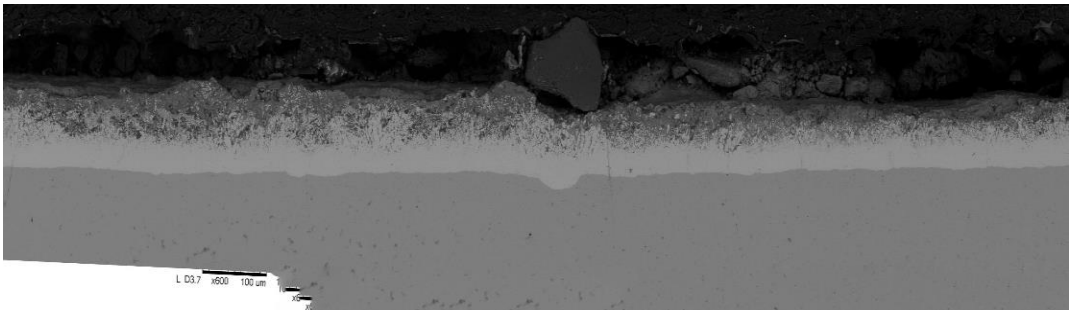


Figure B4 Material 4 sacrificial coupons exhumed after 6 months

# Vita

Diana Cabrera was born in El Paso, Texas and graduated from Father Yermo High School in 2012. She received the degree of Bachelors of Science in Civil Engineering in The University of Texas at El Paso (UTEP) in the fall of 2016. As an undergraduate, she was a peer leader, where she tutored students on lower division engineering courses. After that, she decided to become a research assistant at the Center for Transportation Infrastructure Systems (CTIS). On the fall of 2016, she was a recipient of the Dwight D. Eisenhower Transportation Fellowship, which led her to pursue her Master of Science in Civil Engineering. She enrolled on the master's program at UTEP under the guidance of Dr. Soheil Nazarian.

At CTIS, Ms. Diana mainly worked in a Texas Department of Transportation (TxDOT) project related to MSE walls. She also participated in other TxDOT projects, such as one related to soil stabilization. Although she possessed a strong background in geotechnical engineering, she became interested in transportation after she attended the Transportation Research Board (TRB) annual meeting three times in a row (2015-2018): two times as a Dwight D. Eisenhower Transportation fellow and ultimately as a TRB Minority Student Fellow, where she participated as a lectern session presenter. She also held officer positions in several student organizations such as the American Society of Civil Engineers (ASCE), Transportation Leadership Council (TLC), and Chi Epsilon National Civil Engineering Honor Society. She completed a Master of Science in Civil Engineering in the summer of 2018.

Contact Information: dacabrera6@gmail.com

This thesis was typed by Diana Alejandra Cabrera.